Deliverable 16.5: MAGIC - T3

Initial synthesis of experimental data for calibration and validation of multiscale models in Task 4

Work Package 16

This project has received funding from the European Union's Horizon 2020 research and innovation programme 2014-2018 under grant agreement N°847593.

Document information

Project Acronym	**EURAD**
Project Title	**European Joint Programme on Radioactive Waste Management**
Project Type	**European Joint Programme (EJP)**
EC grant agreement No.	**847593**
Project starting / end date	**1st June 2019 – 30 May 2024**
Work Package No.	**16**
Work Package Title	**Chemo-Mechanical AGIng of Cementitious materials**
Work Package Acronym	**MAGIC**
Deliverable No.	**16.5**
Deliverable Title	**Initial synthesis of experimental data for calibration and validation of multiscale models in Task 4**
Lead Beneficiary	**PSI**
Contractual Delivery Date	**October 2023**
Actual Delivery Date	**January 2024**
Type	**Report**
Dissemination level	**L**
Authors	**Hailing Shi, Thomas Rougelot, Jianfu Shao (LaMcube)** **Mejdi NEJI, Charlotte Dewitte (IRSN)** **Bin Ma, Michele Griffa(EMPA), Sergey Churakov (PSI)**
To be cited as:	Shao J.F., Shi H.L., Rougelot T., Neji M., Dewritte C., Ma B., Griffa M., Churakov S. (2024): Initial synthesis of experimental data for calibration and validation of multiscale models in Task 4. Final version as of 26.01.2024 of deliverable D16.5 of the HORIZON 2020 project EURAD. EC Grant agreement no: 847593.

Disclaimer

Acknowledgement

This document is a deliverable of the European Joint Programme on Radioactive Waste Management (EURAD). EURAD has received funding from the European Union's Horizon 2020 research and innovation programme under grant agreement No 847593.

Status of deliverable		
	By	Date
Delivered (Lead Beneficiary)	Jian-Fu Shao (CNRS)	Dec 2023
Reviewed (internal review)	MAGIC board members	Jan 2024
Verified (WP Leader)	Alexandre Dauzères (IRSN)	Jan 2024
Reviewed (Reviewers)	Janez Perko	Jan 2024
Approved (PMO)	Bernd Grambow	Jan 2024
Submitted to EC (Coordinator)	Andra (Coordinator)	29/01/2024

Executive Summary

This report provides an initial synthesis of experimental data obtained in Task 3, which are devoted to calibration and validation of multiscale models developed in Task 4.

The major achievements of the Task 3 in the WP-MAGIC described in the report include:

- The microstructure evolution of cement paste due to chemical degradation is characterized.
- Development of a new experimental device in view of conducting uniaxial and triaxial compression tests with micro-tomography monitoring.
- Realisation of uniaxial and compression tests with micro-tomographic imaging on mortar samples subjected to three different states of carbonation.
- Non-uniform distributions of strains in the tested samples are determined by using a digital voxel correlation method (DVC).
- The basic mechanical behaviour of mortar and impacts of carbonation processes are analysed.
- The evolution of mechanical properties is estimated for HCP and concrete by micro-indentation measurements.

The presented work is a collective effort of the several research groups, in particular CNRS/LaMcube, IRSN and PSI.

Table of content

List of Figures

List of Tables

Glossary

AAR	Alkali aggregate reactions
ASR	Alkali silica reactions
ASTM	American Society for Testing and Materials
ATP	Adenosine Triphosphate
BSA	Biogenic sulmhuric acid
CASH	Calcium Aluminate Silicate Hydrates
CDF	Cumulative Distribution Function
CEBAMA	Cement Based Materials
CEM	Cement (CEM I, CEM II…)
CFL	Courant-Friedrichs-Lewy
CH	Calcium Hydroxyde: Portlandite
CI	Cement-clay Interaction
CIGEO	Industrial Centre for Geological Disposal
CKD	Cement Kiln Dust
CNT	Classical Nucleation Theory
CORI	Cement Organic Radionuclide Interactions
COX	Callovo-Oxfordian clay
CSH	Calcium Silicates Hydrates
DDL	Diffuse double layer
DEM	Discrete Element Method
EC	European Commission
EDS	Energy dispersive spectroscopy
EPS	Extracellular Polymeric Substances
ESEM	Environmental Scanning Electron Microscopy
EU	European Union
EURAD	European Joint Programme on Radioactive Waste Management
FDM	Finite Difference Method
FE	Finite Element
FEM	Finite Element Method
FFT	Fast Fourier Transform

GC	Gouy-Chapman (model)
GDF	Geological disposal facilities
GEM	Gibbs Energy Minimization
HCP	Hydrated Cement Paste
HET	Heterogeneous
HLW	High-Level Waste
HON	Homogeneous
HPF	Hyperalkaline Plume in Fractured Rock
ILW	Intermediate Level Waste
ISA	Iso-Saccharinic Acid
ITZ	Interfacial Transition Zone
LAC	Low Alkaline Cement
LB	Lattice Boltzmann (method)
LBM	Lattice Boltzman Modelling
LCS	Long-Term Cement studies project
LLW	Low Level Waste
LMA	Law of Mass Action
MAGIC	The chemo-mechanical aging of cementitious materials
MGC	Modified Gouy Chapman model
MICP	Microbial induced calcite precipitation
MS	Member states
MSH	Magnesium Silicate Hydrate
NN	Neural Networks
NRUS	Nonlinear Resonant Ultrasound Spectroscopy
NS	Navier-Stokes
OPA	Opalinus Clay
OPC	Ordinary Portland Cement
PB	Poisson Boltzmann
PDF	Probability Density Function
R&D	Research and Development
REV	Representative Elementary Volume
RH	Relative humidity

RUS	Resonant Ultrasound Spectroscopy
SEM	Scanning Electron Microscope
SNT	Supersaturation-Nucleation-Time
SOB	Sulphur-oxidizing bacteria
SOTA	State of the art
SRB	Sulfate reducing bacteria
THM	Thermo-hydro-mechanical
URL	Underground Rock Laboratory
VFA	Volatil fatty acids
XAS	X-ray absorption spectroscopy
XRD	X-ray diffraction analysis

Introduction

Cementitious materials are widely used in repository design, as structural support material for access galleries, disposal drifts or cells (e.g., concrete/shotcrete), and massive plugs for the sealing of repository infrastructure. The mechanical behaviour of cementitious materials is strongly influenced by repository in situ conditions, the boundary conditions imposed by the geo-technical system and the host rock (i.e. water saturation, temperature, etc.), during both the operational phase and the post-closure transient period. To assess the performance of the cementitious components, studies must be extended over long periods of time, considering various operating conditions. Furthermore, over the long-term, cementitious materials subjected to chemical degradations due to ground- and pore-waters, with aggressive chemical ions. The mineralogical and microstructural changes generated by these aggressive environments might have consequences on the mechanical behaviour and transport properties of the cement matrix.

In Task 3 of WP MAGIC, the bio-chemo-mechanical models for microstructure evolution of cement paste and mortar exposed to various representative disturbances such as carbonation and leaching relevant to the conditions in deep geological nuclear waste repositories are developed and validated using experimental characterisation and multiscale modelling benchmarks.

Moreover, the experimental data obtained in Task 3 are also devoted to be used for the calibration and validation of multiscale models developed in Task 4. For this purpose, the aim of this technical report is to provide an initial synthesis of experimental results so far obtained.

Part Ⅰ Microstructure evolution analysis

1. Objective

Empa and PSI collaborate in subtask 3.1 to investigate different aspects of the chemo-mechanical characterization of cement pastes' microstructure. Their shared objective is to gather essential experimental data for developing a model that accurately captures the evolution of the pastes' microstructure at the micro scales. These data serve as input for upscaling and model parametrisation in subtasks 3.4, as well as for large scale simulations and couplings in Task 4.

2. Material

The project partners at PSI and Empa work with mortar specimens (0.1 – 0.3 mm sand sieve size), based upon the same cement types (i.e., ESDRED and OPC) as the aged mortars/concretes from the CI experiment, also investigated in Task 2 on a larger scale, see Table 2-1 and Table 2-2 for the respective mix designs. Such specimens need to be exposed to the (synthetic) Opalinus Clay (OPA) pore solution (see Table 2-3 for the composition and recipe), for realizing accelerated degradation conditions, by hosting each specimen inside an in-house designed and manufactured diffusion cell, acting as a chemical degradation reactor. To achieve the experimental, objectives 30 reactors systems were setup. The cell's design also required additional design modifications for 6 of the 30 cells, i.e., for those to be used in the measurements of the diffusivity, in order to minimize risks of film/corner flows along the interface between the inner PCTFE mould and its PTFE external holder.

Table 2-1: mix design of the OPC mortar (see interface system 2277 in Subtask 2.2)

Component	**Type**	**Content (kg·m^{-3})**
Cement	CEM I 42.5 N HS ("Protégé 4R" by Holcim Switzerland)	899
Water	Tap water	423
Aggregate	Quartz sand♦, 0.1 - 0.3 mm sieve size range	728

♦ By Bernasconi AG, product name Quarzsand N

Table 2-2: mix design of the ESDRED mortar (see interface system 2278 in Subtask 2.2)

Component	**Type**	**Content (kg·m^{-3})**
Cement	CEM I 42.5 N ("Normo 4" by Holcim Switzerland)	495
Supplementary Cementitious Material (SCM)	Silica fume ("SikaFume HR/TU" by Sika Switzerland), 100 nm average grain diameter	332
Water	Tap water	411
Aggregate	Quartz sand♦, 0.1 – 0.3 mm sieve size range	573
Additive 1	Superplasticizer ("MasterGlenium ACE 331" by MasterBuilders Solutions)	9.7
Additive 2	Accelerator ("Sigunit L53 AF" by Sika Switzerland)	40

♦ By Bernasconi AG, product name Quarzsand N

Table 2-3: Composition and recipe of the Opalinus Clay pore water solution (Mäder et al., 2018)

	Pore solution composition		**Recipe**	
Species	**mg/L**	**mmol/L**	**Compound**	**g/L**
Na	5540	241.0	NaCl	12.393
K	56.5	1.45	$NaHCO_3$	0.044
Ca	582	14.52	$CaCl_2 \cdot 2H_2O$	2.134
Mg	399	16.41	KCl	0.108
Cl	9763	275.4	$MgCl_2 \cdot 6H_2O$	3.337
SO_4	1365	14.21	Na_2SO_4	2.018
HCO_3	32.1	0.53		
pH (lab, 25 ºC)	8.08			
pH (cal., 25 ºC)	7.88			

3. Methods

The diffusion experiment was executed utilizing a HTO tracer to probe the accessible porosity of the mortar. A standard through-diffusion setup was employed, involving the assembly of a diffusion cell. The cell comprised a high concentration reservoir where the HTO tracer was introduced and a low concentration reservoir, containing solely the clay pore solution, which was regularly replenished to sustain an almost negligible concentration of HTO. A peristaltic pump circulated the solution on both sides to ensure uniform concentration. Consequently, a concentration gradient of HTO was established between the high and low concentration reservoirs, initiating well-defined molecular diffusion. Over time, samples were collected from both the high and low concentration reservoirs. The same configuration was employed for the degradation experiment, differing only in the absence of HTO in the high concentration reservoir. Both diffusion and degradation experiments are performed at 40°C, to mimic the underground temperature.

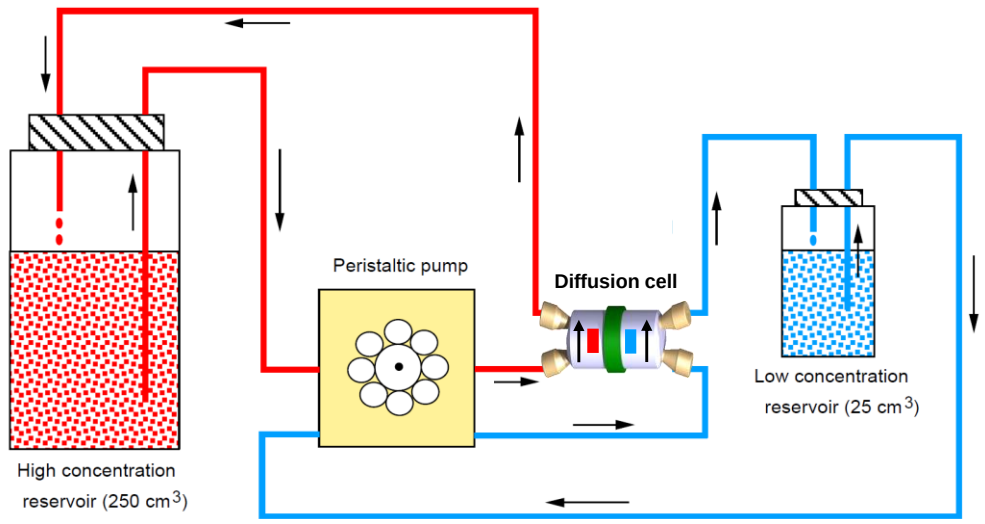

Figure 3-1: Scheme of the experimental set-up of the through-diffusion experiment using the newly designed diffusion cell. The same set-up is used for the degradation experiment; the only difference is without adding HTO in the high concentration reservoir.

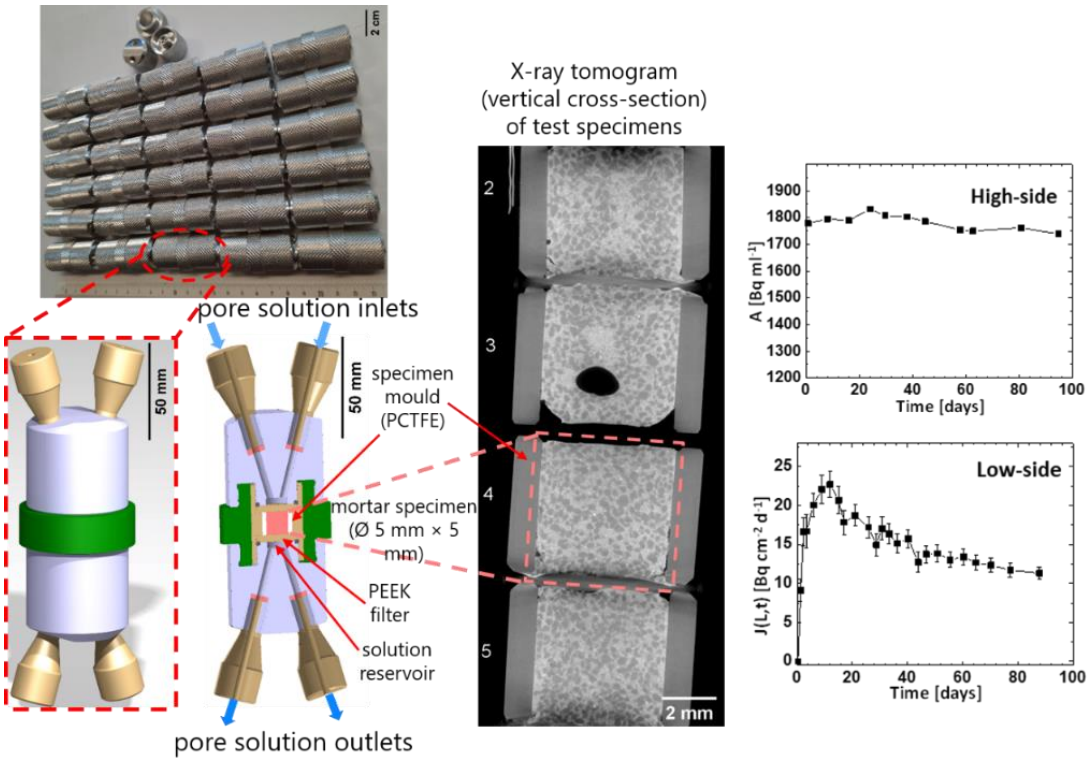

Figure 3-2: Left column: manufactured flow cells (top photo) according with the new design (bottom solid drawings). Middle column: a vertical cross-section from the X-ray tomogram of four vertically stacked OPC mortar specimens. Right column: HTO activity (A) in the high-concentration side (top plot) and its diffusive flux density (J) at the low-concentration side (bottom plot), both as functions of time.

Further, the development was focused on the optimization of the casting for small mortar specimens. The Figure 3-2 shows an example of distinct OPC mortar (w/b = 0.47) specimens cast in the PCTFE moulds, as visible in a vertical cross-section of an X-ray tomogram acquired at 28 days. As visible in the case of specimen Nr. 3, the initial casting approach was not optimal, because samples contain air, while the one of specimen Nr. 4 allowed avoiding both such air entrapment and detachment of the material from the mould due to autogenous and drying shrinkage. In the next step the tomography measurement settings were optimised examination of visible (resolution in a scale of microns) defects (e.g., boundary cracks or air voids) within the mortars or gaps between the mortar and the mould wall, to be used for quality control before starting the full experimental campaign.

The time-lapse poro-mechanical characterization during the ongoing degradation are twofold.

On the one side, for each mix design, three specimens are taken periodically (every 6 months, for a total of six time points) out of the respective cells and their complex-valued (i.e., viscoelastic, storage + loss) linear Young and shear moduli will be estimated. Such estimates are obtained by performing MUlti-MOde Resonant Ultrasound Spectroscopy (MUMORUS) measurements and by solving the corresponding inverse problem (Zadler et al., 2004). While the measured resonance frequencies allow estimating the storage moduli, the loss moduli are estimated from the Q-factor values of the resonance peaks (Zadler et al., 2004). On the other side, at the same time points, the diffusion coefficient of HTO (Luraschi et al., 2020) for three distinct specimens are measured and adopted both as a degradation proxy variable and as a quantitative parameter to assess the pore space changes. The two measurement types cannot be performed on the exactly the same exact specimens: due to activation of the sample by HTO's decay, the three specimens for the diffusion measurements are not be able to leave the radiation-safe labs at PSI, where the MUMORUS setup cannot be hosted. The microstructure evolution is assessed, on the one side, non-destructively by X-ray tomography performed on the same specimens for the mechanical characterization and at the same exact time points. On the other side, at each of four time points during the whole duration of the experimental campaign, one of the additional specimens is sacrificed for inspecting the microstructure at smaller scale by SEM. The same

impregnated and polished cross-section, as used for SEM, are subjected to EDX mapping, in order to assess both the elemental composition and its spatial-temporal evolution. Additional specimens are sacrificed for powder XRD (PXRD) analysis, in order to assess changes in some cement hydrates.

4. Results

Using a first prototype of the newly designed cell and the specimen of Nr. 4, a first HTO diffusion experiment has been conducted at 40°C, with the goal of assessing the suitability of the designed cell for accelerated mortar degradation. The initial HTO diffusion results are shown in the right column of Figure 3-2. After around 16 days, the flux in the low concentration side reached the maximum and then decreased continuously with time. The decrease may be caused by progressing carbonation, in that the newly formed calcite may change the pore structure of the mortar. The latter is the subject of investigation by the time-lapse tomography measurements.

All the originally planned 30 reactors are manufactured and collected at Empa and PSI. Six reactors (3 for each mortar type) are specifically dedicated to measurement of the temporal evolution of the diffusion coefficient at PSI Hotlabor, by using tritiated water (HTO) as a radioactive tracer. The most critical and time consuming part of the instrumental development and testing was the manufacturing and assembly of components for the resonant ultrasound spectroscopy (RUS) rig, shown in Figure 4-1(a), used for the for the visco-elastic moduli measurements.

At the time of reporting, all cylindrical specimens, with a size of ø 5 mm × 5 mm, are curing in the corresponding sleeve moulds of the diffusion cells. Additionally, several square prisms, both with a larger size of 25 mm × 25 mm × 100 mm, as well as prisms with size 5 mm × 5 mm × 40 mm (shown in Figure 4-1 (b)), were also cast, for each mortar type, as specimens for further validation and for comparison of the (visco-)elastic moduli estimation on the tiny ø 5 mm × 5 mm cylinders. The latter estimation by the solution of the RUS inverse problem is a challenging task requiring extensive validation. After 3 weeks curing, X-ray tomography has been applied to inspect the cast specimen and to select those with no defects at the scale of tens of microns. It is essential to confirm that the sample do not contain air voids, porous patched of similar size and extensive delamination between the cast cylinder and the mould's inner surface. Figure 4-1 (c) shows one vertical cross-section for the tomogram of 6 of the newly cast OPC mortar specimens. Specimen Nr. 6 was, for example, not selected for the time-lapse X-ray tomography + RUS measurements because containing a large air void, which would strongly perturb and slow down the OPA pore solution diffusion, in addition to make the mechanical characterization less meaningful, because of its large vol.-%.

All the flow cells, equipped with the new freshly cast specimens, are set up for both the degradation acceleration and the diffusion coefficient measurements at 40°C. The RUS and X-ray tomography measurements of the degraded mortars are scheduled for every 6 month, some of the specimens will be sacrificed for XRD and SEM-EDX analysis. At each time point, HTO through-/out-diffusion experiments are also performed. After contacting with the OPA clay pore solution for 1.5 months, the degraded mortars were measured with RUS and X-ray tomography for the first time point. In the same month, HTO through-diffusion experiments were started, to determine the accessible micropores during the degradation. The through-diffusion curves for OPC or ESDRED-based mortars were obtained, showing that the steady state was reached after ~12 days diffusion (Figure 4-2). Compared to OPC mortars, higher flux of HTO was observed in ESDRED mortars under the same diffusion experiment conditions, indicating a larger effective diffusion coefficient (De) for ESDRED. Further modelling (e.g., by COMSOL) on the diffusion data will be conducted (e.g., by COMSOL), to derive the specific values of De and rock capacity. Out-diffusion experiments conducted after the in-diffusion study are used to confirm the through-diffusion results and for detecting possible dual-porosity microstructure. Besides, already aged, corresponding mortars from the CI experiment will be characterized also at this length scale range, in terms of mechanical-chemical-mineralogical properties, as a link between what was done In Task 3 at microscopic scale and what was done in Task 2 at the macroscopic scale.

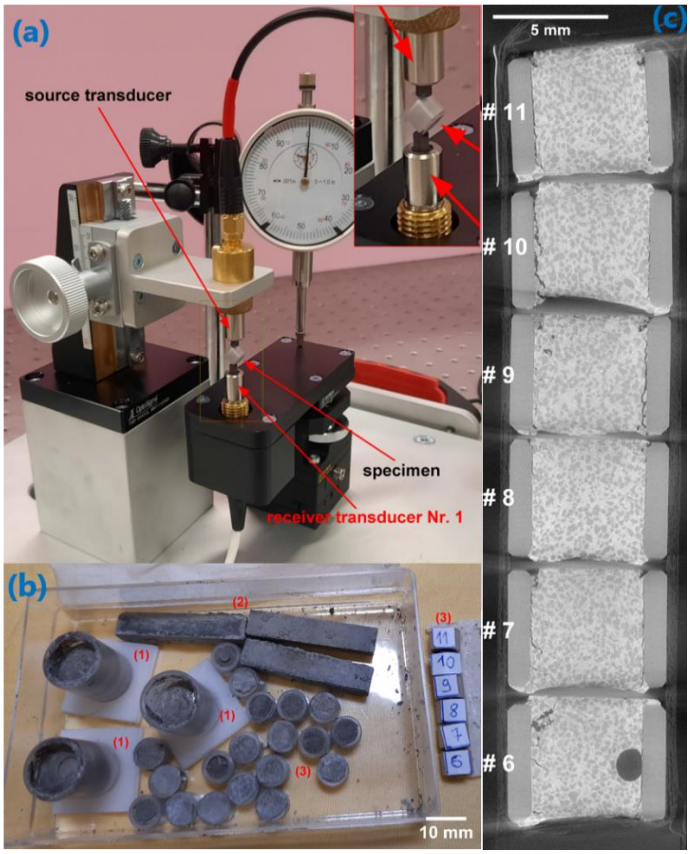

Figure 4-1: (a) Resonant Ultrasound Spectroscopy (RUS) rig implemented by PSI/Empa for the time-lapse (visco-)elastic moduli measurements on the Ø 5 mm × 5 mm mortars specimen cast within PCTFE moulds, one example of which is visible in the zoom-in at the top-right corner, while being clamped between the ultrasound vibration source transducer and a receiver one; (b) examples of newly cast mortar specimens (of OPC type), with (1) indicating those for diffusion coefficient measurements, (2) those for validating the RUS measurements and (3) the same cylindrical specimens as in (a) for the actual time-lapse campaign; (c) vertical cross-section from the X-ray tomogram of a columnar stack of 6 cylindrical specimens (those labelled with corresponding numbers in (b)), acquired for the selection of specimens without large air voids (as in # 6) and/or extensive delamination of the mortar-mould interface (as in # 10).

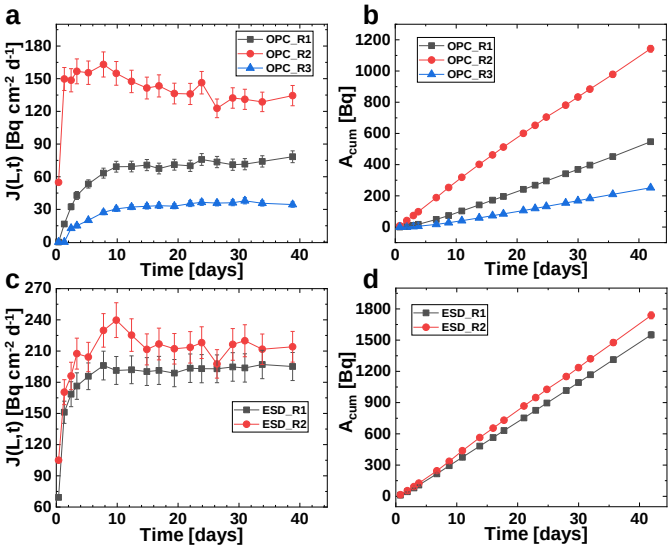

Figure 4-2: Flux (a, c) and accumulated radioactivity (b, d) at the zero-concentration boundary of HTO through-diffusion in two types of mortars: (a, b) OPC-based and (c, d) ESDRED-based ones. OPC_R1, OPC_R2, and OPC_R3 are the three replicates for the OPC mortar. ESD_R1 and ESD_R2 are two of the triplicates for the ESDRED mortar, with the third replicate failed.

5. Summary & conclusion

Empa and PSI collaborate on subtask 3.1, focusing on chemo-mechanical characterization of cement pastes' microstructure for model development. Mortar specimens, exposed to Opalinus Clay pore solution, undergo diffusion and degradation experiments at 40°C. The newly designed reaction cell was employed for diffusion experiment and accelerated degradation experiment. Initial HTO diffusion results reveal potential effects of carbonation on mortar pore structure. Despite initial delays with delivery of components, reactors for time-lapse experiments are ready, including resonance spectroscopy for viscoelastic moduli measurements. In conclusion, the collaborative efforts of Empa and PSI in subtask 3.1 have successfully laid the groundwork for in-depth investigations into cement paste microstructure. The available HTO breakthrough curves can be used for the validation of transport models. Despite initial challenges in cell design and component delays, the diffusion and degradation experiments are underway, revealing early insights into potential carbonation effects. The comprehensive approach, combining resonance spectroscopy, X-ray tomography, and SEM-EDX mapping, promises a detailed understanding of microstructure evolution. As the experiments progress, further analyses will refine models and contribute valuable data to the broader context of cement degradation. The commitment to ongoing measurements and analyses demonstrates a dedication to advancing the understanding of chemo-mechanical interactions in cement pastes.

RUS measurements, X-ray tomography, and SEM-EDX mapping at the starting time point of the degradation experiments have been performed to provide comprehensive insights into microstructure evolution. Future data processing and result analyses will be done after the final report. Sampling and comprehensive characterizations for the following 4-5 time points will be continued. Eventually, all the results will be concluded into peer-reviewed article publications.

Part Ⅱ Meso-mechanics experiments

6. Experimental device and methodology

6.1 X-ray micro-tomography

LaMcube has performed uniaxial and triaxial compression tests on mortar samples with micro-tomography monitoring. X-ray micro-tomography is a versatile and non-destructive imaging tool that aims at obtaining a three dimensional map of X-ray absorption coefficient of the material components. Basically, the sample is irradiated by a beam coming from an X-ray source. A generally planar detector measures the transmitted intensity. A 2D projection (radiograph) of the sample is therefore obtained, containing information on average attenuations along the different paths from source to detector through the material. Then, this acquisition is performed for various angles. Usually, the sample is rotated step by step to a fraction of degree around its vertical axis until a 180 or 360-degree turn is complete. The series of acquired 2D radiographs allows a 3D reconstruction through different existing computational methods as filtered back-projection algorithm for instance (Kak and Slaney, 2001). The image contrast depends on the relative attenuation of the objects in the sample. After the X-ray emitted by the signal source penetrates the object, the attenuated signal conforms to the following attenuation equation (Latiere and Mazerolle, 1987):

$$I = I_0 \exp(-\mu l) \qquad (1.1)$$

Where: I is the attenuated intensity X-ray, J/(cm^2·s), I_0 is the incident intensity of X-ray, J/(cm^2·s), μ is the absorption coefficient of the substance irradiated by X-ray, l is the thickness of the object.

The resolution of this 3D map of attenuation highly relies on the configuration of the performed acquisition: size of the sample, size of the focal spot, size of the detector, magnification used (ratio between the sample-to-detector and the sample-to-source distances), etc. In addition, the X-ray attenuation of a given constituent is linked to its chemical (atomic number) and physical (density and thickness) properties and to X-ray energy (Attix, 2004). The attenuation contrast between the constituents should be high enough to be able to identify the microstructure.

Acquisitions have been performed at the In Situ Innovative Set-ups under X-ray Micro-tomography (ISIS4D) (Limodin et al., 2013) platform (see Figure 6-1) using a computed tomography system Ultra Tom$^{\bigcirc,R}$ from RX Solutions. This device allows scanning a wide range of material samples and sizes (from hundreds of micrometres up to several tens of centimetres) under various loading conditions thanks to the different X-ray generators, detectors, in situ devices and parameters of acquisition.

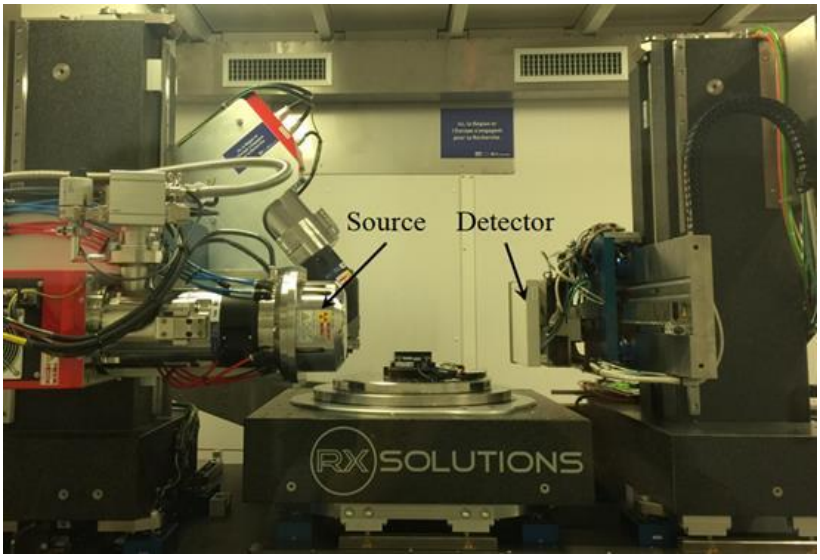

Figure 6-1: In Situ Innovative Set-ups under X-ray Micro-tomography (ISIS4D) platform.

For this study, the X-ray source is a nanofocus X-ray tube from Hamamatsu. The operation voltage was set at 80 kV in order to discern the constituents of the mortar sample. To achieve a voxel size of about 7 µm required to investigate its microstructure and its evolution under different loading levels, the filament current was set to 85 µA (maintaining the focal spot of the X-ray cone beam smaller than the resolution) and the geometrical magnification was a compromise between diameter of the specimen and duration of each acquisition. The specimen, placed the closest to the source, has a diameter limited to 5 mm, a flat-panel detector (1880x1496 pixels, pixel size 127 µm) has been selected and 1120 radiographs were taken through a 360-degree turn. Six images were averaged at a given angular position to reduced noise. The reconstruction of the tomographic data is performed with a filtered back-projection algorithm using X-act©,® software.

6.2 Triaxial and creep devices

A particular mechanical device has been used here allowing the application of uniaxial and triaxial compression on the X-ray micro-tomography platform. This mechanical device mainly consists of a metal indenter, a metal base and a long cell made of a highly transmissive polycarbonate. Its internal components are shown in Figure 6-2 (Shi et al., 2023) and the parts in contact with the sample are made of the same material (polycarbonate) as the cell to reduce the influence on the 3D reconstructions of the images. It provides a stable and long-term compressive pressure on the sample during the test. As opposed to conventional laboratory tests, X-ray microtomography coupled with DVC replaced conventional local measurements such as strain gauges and Linear Variable Differential Transformers (LVDTs) to have 3D maps of strains throughout the sample at different loading steps or time. This device is designed for various compression tests on samples with a maximum diameter of 5 mm and a length of 10 mm. It can provide a confining compressive pressure of up to 6 MPa in triaxial tests.

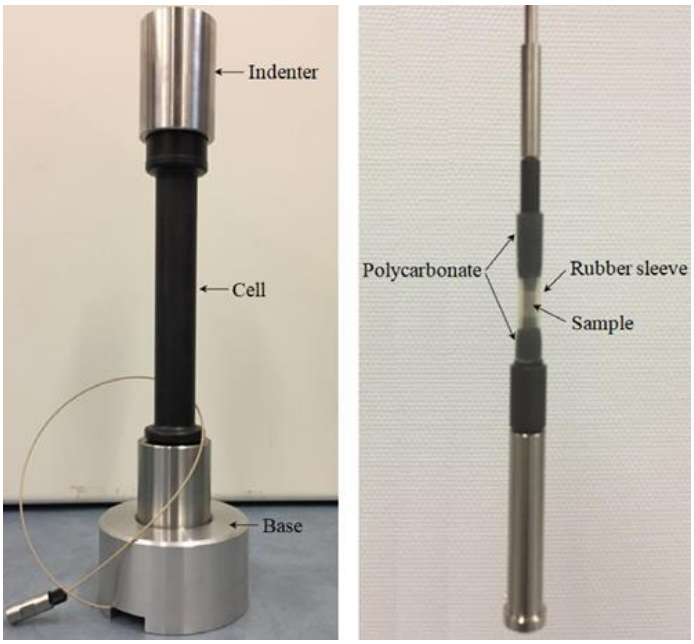

Figure 6-2: The triaxial device employed for in situ uniaxial and triaxial compression tests.

In order to realize in situ uniaxial creep compression tests with X-ray micro-tomography, a new experimental device was developed. As shown in Figure 6-3 (Shi et al., 2021), the designed device includes a long cell, a manual axial loading system, a base, a force sensor and a data logger. The long cell is made of polycarbonate with a high light transmissibility for X-ray. It also has a good mechanical stability. The force sensor has an accuracy of 0.01 kg and a range of 0-100 kg. For the specimens with a diameter of 4-5 mm studied here, the maximum of axial stress generated is about 60-80 MPa. In Figure 6-3, one can see the sample is sandwiched at the middle part of cell by a pair of translucent polycarbonate bases to minimize the friction at the upper and lower surface with loading system. The axial stress is increased as slowly as possible and is monitored by the force sensor. During creep stage, the axial force is regularly adjusted to keep the loading constant.

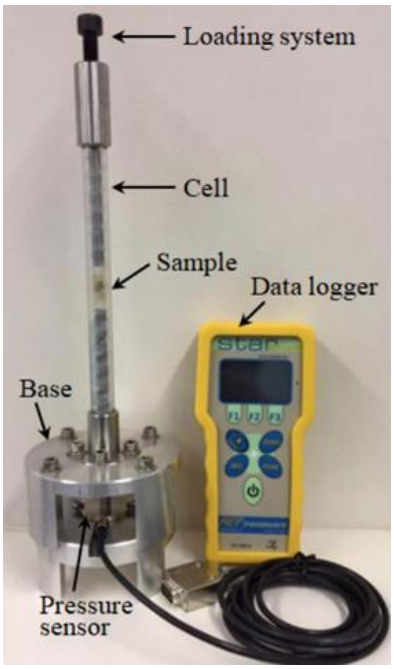

Figure 6-3: The creep device employed for in situ uniaxial compression creep tests.

6.3 Digital volume correlation

Digital Image Correlation (DIC) is a technique for measuring displacements on surfaces under different load conditions (Sutton et al., 1983). The basic idea is to compare two images of the same zone between two subsequent states, and then to compute the displacement and strain fields in the zone by searching for the best match between the images. Three-dimensional Digital Volume Correlation (DVC) methods are an extension of the two-dimensional DIC methods (Buljac et al., 2018). Significant advances have been achieved since the end of 1990s and these methods are now widely used for quantitative treatment and analysis of 2D and 3D images. Only a short review is presented here.

Each image is identified by its gray scale function representing the volume of the sample. Let f denoting the reference 3D image taken before the deformation, while g the deformed 3D image taken after the deformation. In the present study, we use the optical flow equation, which assumes that the gray scale variations are only due to the displacement of the material point:

$$g(\vec{x}) = f[\vec{x} + \vec{v}(\vec{x})] \qquad (1.2)$$

where $\vec{x}$ is the vector denoting the position of the voxel and $\vec{v}$ is the related displacement vector.

In this study, DVC is carried out with YaDICs software, developed in Laboratoire de Mécanique Multiphysique Multiéchelle (LaMcube) of Lille, France (Seghir et al., 2014). The platform is based on C++, and optimized to process 3D volumes in a reduced time. To identify displacements, several parameters have to be defined: a metric, a sampling, an interpolator, a transformation, an optimizer and finally a regularization method (see Figure 6-4). More details can be found in https://yadics.univ-lille1.fr/wordpress/index.html.

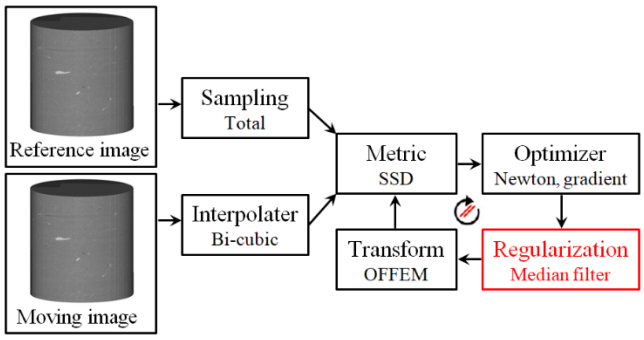

Figure 6-4: Different steps of DVC process with YaDICs software (Shi et al., 2023).

Displacements can be searched using a decomposition on a discrete basis:

$$\bar{u}(\bar{x}) = \sum a_n \bar{\psi}_n(\bar{x})] \qquad (1.3)$$

with a_n, the sought degrees of freedom and $\bar{\psi}_n$, the shape functions. In this study, finite elements method shape functions are used (Besnard et al., 2006), providing a continuous displacements field on the whole studied volume. An interest is to present the same formalism for numerical simulations so that interpolation errors can be reduced for material parameters identification for example (Avril et al., 2008).

A multi-scale resolution strategy is adopted for the DVC. This pyramid scheme reduces the problem size and thus avoids some local minimum traps. In the present case, six scales, i.e. resolutions, are employed; the coarsest one is the 'scale 5' with one 'macro' voxel, which is averaged over $2^5 \times 2^5 \times 2^5$ voxels while the full resolution image corresponding to a volume of $2^0 \times 2^0 \times 2^0$ (see Figure 6-5).

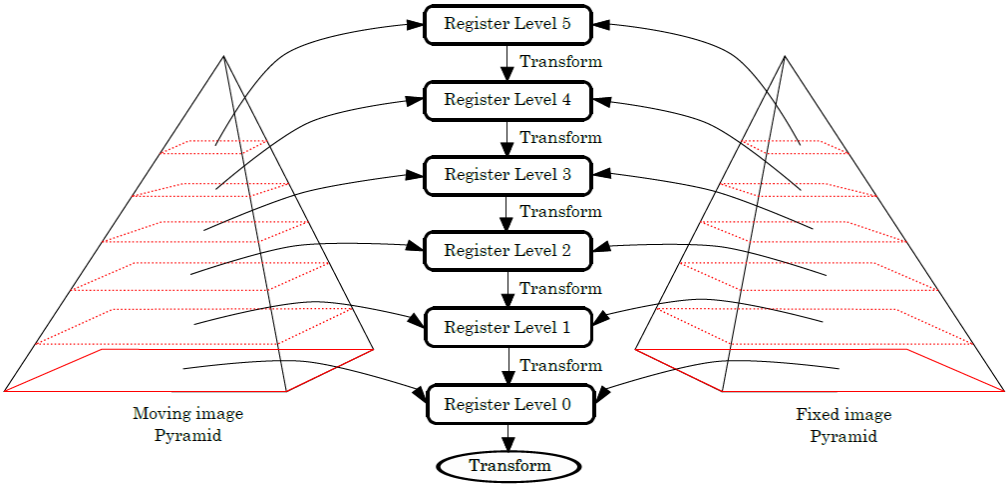

Figure 6-5: Pyramidal process employed in YaDICs (Shi et al., 2020).

Choosing the most suitable element size is very important for the results of DVC calculation. The results of the local strain calculation show a diffusion phenomenon, i.e., the larger the element size, the more obvious the diffusion phenomenon around the local deformation. The uncertainty of displacement field is widely used as a parameter to evaluate the accuracy of calculations with DVC methods. This uncertainty is calculated by the standard deviation of the displacement between the two pictures. One is at the reference position and the other translated of few microns. Then, the standard deviation of the displacement field is calculated for all the components in three directions. Figure 6-6 (for triaxial device) and Figure 6-7 (for creep device) show the evolution of uncertainty for the three displacement components when the element size varies from 4 to 64 voxels. Although the uncertainty for high spatial resolution is several times higher than that of low resolution, the description of strain localization process is much better. Considering together the results of strain localization, the time cost of the DVC calculations and the uncertainty in displacement field, the element sizes with 4 and 8 voxels is selected in this study for the DVC analysis of all compression tests. Generally, a computational element size of 8 × 8 × 8 pixels is consistently preferred, which is the result of a balance between computational

resources required by DVC and fineness of strain fields. It is also considered to use a computational element size of 4 × 4 × 4 pixels for better strain fields in cases when the computational quantities are not particularly large. It is notable that the uncertainties of the DVC results in these two computational element sizes are less than 0.2 voxel and good local strains are obtained. Data visualization and analysis of both full-field and local strains acquired from DVC computations are supported by Avizo©,® software.

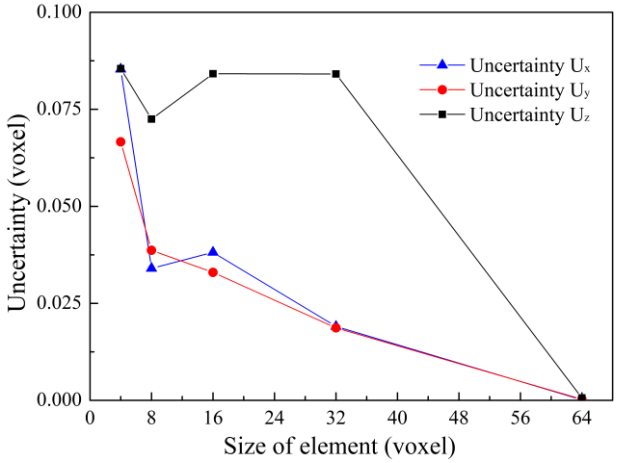

Figure 6-6: Variations of uncertainty for three components of displacement with different element sizes in DVC calculations on the triaxial device (Shi et al., 2023).

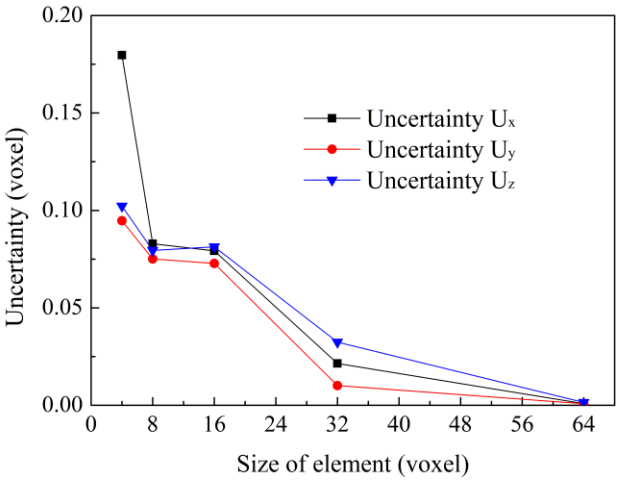

Figure 6-7: Variations of uncertainty for three components of displacement with different element sizes in DVC calculations on the creep device (Shi et al., 2021).

7. Sample preparation

7.1 Production of mortar samples

Samples for micro-mechanical tests were cast according to the parameters provided by LMDC. Here, sand up to 1 mm was used instead of stone as aggregate. Then samples were made according to the informed parameters “Water absorption of sand = 0.5%”, “Efficient water / Cement = 0.579” and “Sand / Cement = 3”. The sand and cement used to produce samples are shown in Figure 7-1. Here a special mould (see Figure 7-2) was custom-made in a nylon plate to produce the mortar samples. The cylindrical holes in the nylon plate have a diameter of about 5 mm and 4 mm and a depth of about 25 mm, with a removable bottom and top cover. Note that while filling the holes with mortar, a needle is required to help the filling and to ensure a first vibration. After filling the holes place the mould on a shaking table for X minutes. Samples initially cured in their mould at room temperature and approximately 100% humidity for 4 days, and then were unmoulded for 24 days. To ensure an initial fully-saturated state, samples were then placed in lime-saturated water. Figure 7-3 shows the demoulded samples being cured in the lime-saturated water.

Figure 7-1: Raw materials used in the production of samples.

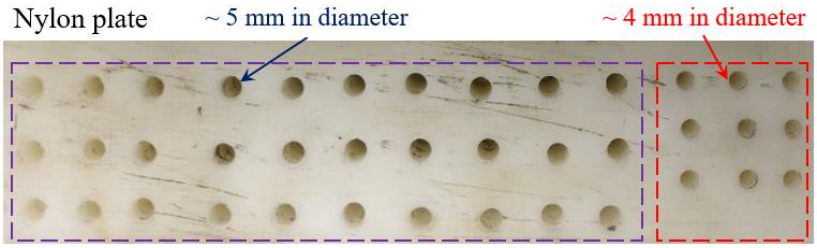

Figure 7-2: The special customized nylon plate mould.

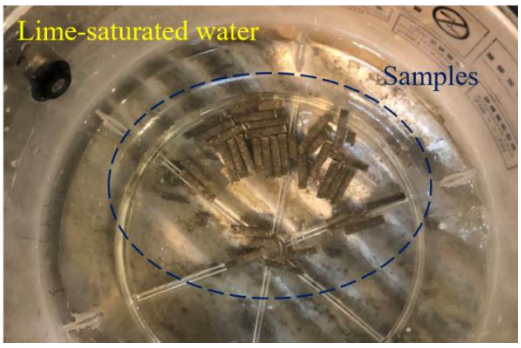

Figure 7-3: Samples were maintained in the lime-saturated water.

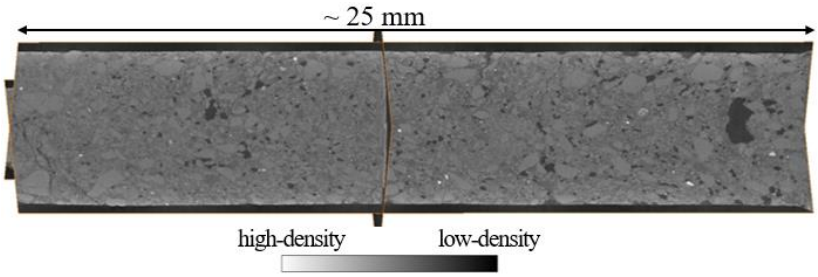

Figure 7-4: Reconstructed X-ray micro-tomographic grayscale image of a mortar sample with “Sand / Cement = 3”.

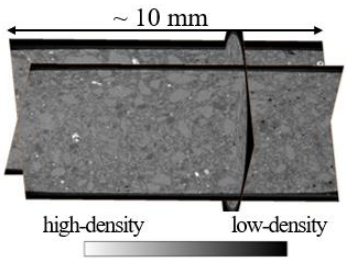

Figure 7-5: Reconstructed X-ray micro-tomographic grayscale image of a mortar sample with “Sand / Cement = 2”.

A maintained mortar sample was scanned by X-ray micro-tomography and the acquired result is shown in Figure 7-4. As can be seen in the image, there are a large number of visible defects (pores) in the sample. Some of the defects even exceed 1 mm. To minimize defects and contraction of hardening in mortar samples, a modification was made to the ratio of sand to cement (from Sand / Cement = 3 to Sand / Cement = 2). A representative X-ray micro-tomographic image of the reproduced mortar samples is presented in Figure 7-5. As can be seen in Figure 7-5, the defects in the sample are significantly reduced with respect to Figure 7-4.

For compression tests, parallelism between both ends of mortar samples (and perpendicularity to the generatrix) is required. Lathe has been used here (see Figure 7-6). Finally, partially formed mortar samples are shown in Figure Figure 7-7.

Figure 7-6: Sample preparation by lathe.

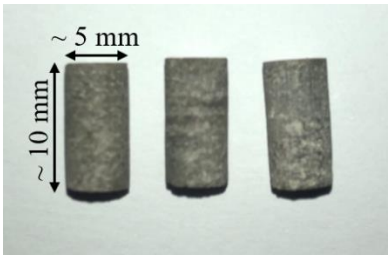

Figure 7-7: Formed mortar samples.

7.2 Carbonation equipment

In this study, the carbonation of the mortar and concrete samples is performed in a modified climatic chamber (see Figure 7-8) that allows for the control of temperature, humidity and carbon dioxide level inside. The carbonation is aimed to be performed at 20°C between 50-65% in Relative Humidity (RH) and 50% CO_2 in a modified climatic chamber (norm XP P 18-458). An additional PMMA box has been built and installed inside the climatic chamber, as shown in Figure 7-8(b)}. Its role is to limit the leaks of CO_2 but also to ensure that the RH inside this box remains in the range of 50% to 65% in RH. A number of holes have been drilled to ensure water vapour exchanges between the climatic chamber and the box. The CO_2 injection is directly performed inside the box. Different trays (with holes) have been installed inside the box to store the different specimens and help increasing the air flow between samples (to get a homogeneous carbonation). If required, a small fan will be added to improve the homogeneity of the carbonation atmosphere throughout the box. The regulation of temperature inside the box is unaffected due to the low thermal insulation of PMMA. The carbonation chamber is now operational.

(a) Carbonation chamber (b) The additional PMMA box

Figure 7-8: Chamber for carbonation of mortar and concrete samples.

8. Test process and current results

8.1 Test progress

As of now, two batches of mortar samples have been completed, partly in curing and partly in carbonation. For the uncarbonated mortar samples, four uniaxial compression tests and three triaxial compression tests were performed on the X-ray micro-tomography platform. Simultaneously, carbonation of mortar and concrete samples has been progressively advancing. After overcoming various difficulties, the operations for carbonization of mortar and concrete samples have been completely mastered. For the carbonation processes of the mortar samples, which are likewise monitored by X-ray micro-tomography. For the carbonised samples, a total of five compression tests were performed. The completion of the tests can be found in Table 8-1. Furthermore, samples S1-2t and S1-10t were monitored for the carbonation process.

Table 8-1: Completion of uniaxial and triaxial compression tests.

Carbonation level / Radial stress	0%	50%	100%
0 MPa	S1-1, S1-2, S1-3, S1-4	S2-4, S2-4s	S1-2t
3 MPa	S1-3s	S1-1s	S1-5c, S1-7c
6 MPa	S1-5, S1-6		S1-10t (failure)

8.2 Results of carbonation

Two mortar samples (S1-2t and S1-10t) were selected to investigate the effects of carbonation. The samples were scanned in their initial state, medium carbonated state and full carbonated state. Samples are carbonated at 20°C, 65% in RH and 50% concentration of CO_2. Positive values of the DVC computed results are defined here as compression and negative values are defined as dilation. To facilitate the observation of compression and dilation zones in strain fields, red colour is defined as compression and blue colour as dilation in this report. It is difficult to observe changes in the samples directly from the reconstructed grayscale images. With the help of the strain fields obtained from DVC computations, the fine variations in samples can be well characterized.

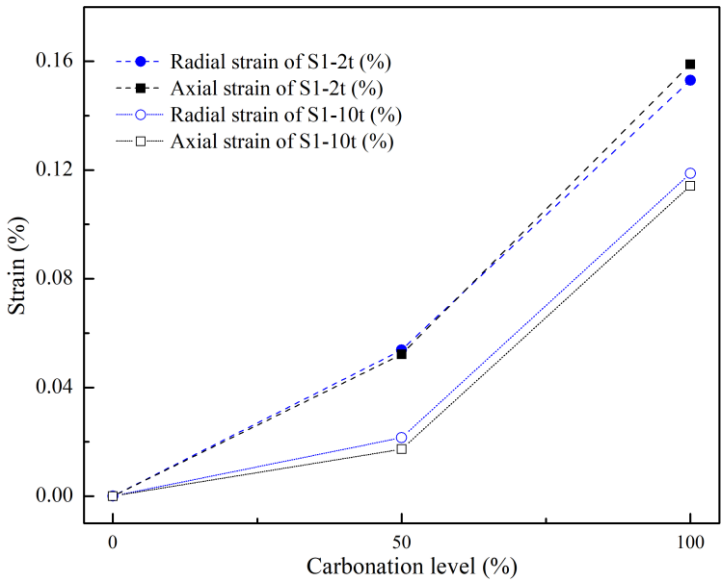

Figure 8-1: Variations of radial and axial strains of the samples S1-2t and S-10t in response to carbonation level.

Figure 8-1 presents variations in the global average radial and axial strains for samples S1-2t and S1-10t at different carbonation levels. One can see that the samples are in a continuous shrinkage state. The overall trend is to be slow and then fast, with the values of radial and axial shrinkage being almost the same. Figure 8-2 and Figure 8-3 illustrate the variations of the strain fields for the internal longitudinal slices of samples S1-2t and S1-10t, respectively. It can be seen that the local shrinkage bands are basically located in the cement portion of the interfacial zone between cement and sand. A few dilation bands (in blue colour) can be observed in the strain fields of sample S1-10t in the initial crack zone. It can be indicated that the cracks expand slightly during the carbonation process of the sample.

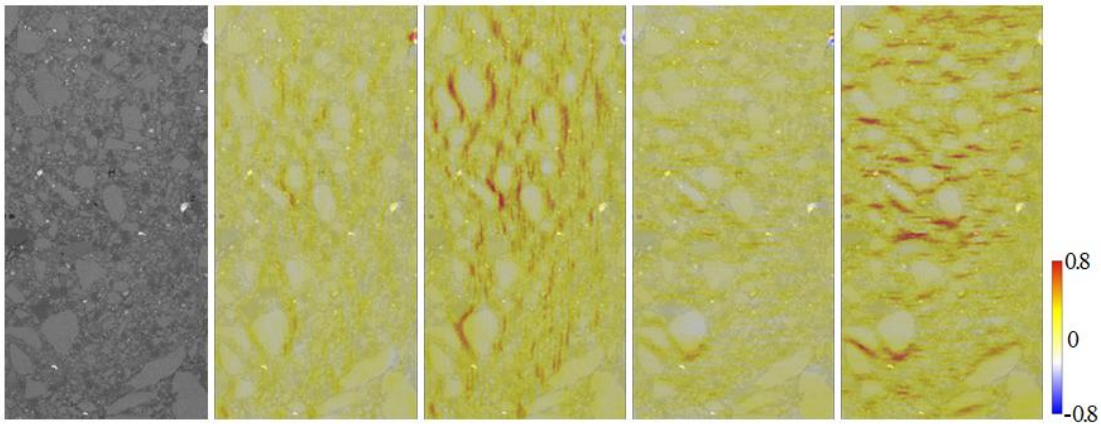

(a) (b) (c) (d) (e)

Figure 8-2: Variations of the strain fields at different carbonation levels for sample S1-2t. (a) Grey scale image of initial state, (b) Radial strain field for medium carbonation (50%), (c) Radial strain field for full carbonation (100%), (d) Axial strain field for medium carbonation (50%), (e) Axial strain field for full carbonation (100%)

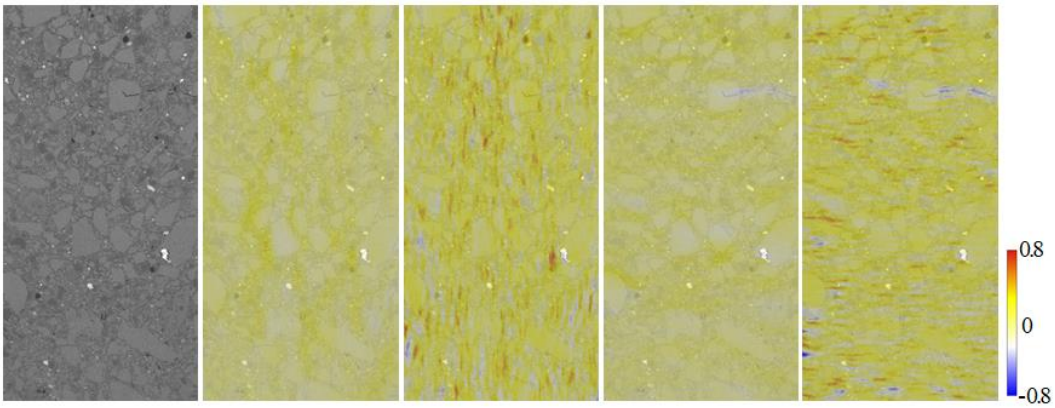

(a) (b) (c) (d) (e)

Figure 8-3: Variations of the strain fields at different carbonation levels for sample S1-10t. (a) Grey scale image of initial state, (b) Radial strain field for medium carbonation (50%), (c) Radial strain field for full carbonation (100%), (d) Axial strain field for medium carbonation (50%), (e) Axial strain field for full carbonation (100%)

8.3 Results of uniaxial and triaxial compression tests

Based on high-contrast 3D tomographic images, DVC approach provides a valuable means for calculating global and local deformations. The reliability and precision of the results are satisfactory, particularly for samples with complex structures and compositions. The results of the first uniaxial compression test on the mortar sample are displayed in Figure 8-4 to Figure 8-7. Figure 8-4 presents the evolution of the average strains (computed by DVC) of the mortar sample in the first uniaxial compression test. Figure 8-5 shows the details of two mutually perpendicular longitudinal slices. Figure 8-6 and Figure 8-7 display the representative accumulated axial and radial strain fields, respectively, of the two selected longitudinal slices in Figure 8-5. To facilitate the observation of compression and dilation zones in strain fields, red colour is defined as compression and blue colour as dilation in this report.

As can be seen from Figure 8-4, the entire uniaxial compression test includes three unloading processes. The axial strains are essentially normal, however the radial strains show an unacceptable deviation. The radial strain values of three re-loadings after unloading are relatively small. After multiple repeated image inspections and verified computations, no reason was found. We therefore performed a uniaxial loading-unloading test on the second mortar sample. The same result was again achieved. The stress-strain figure of the second uniaxial compression test is not presented here as it was not computed for all scan points.

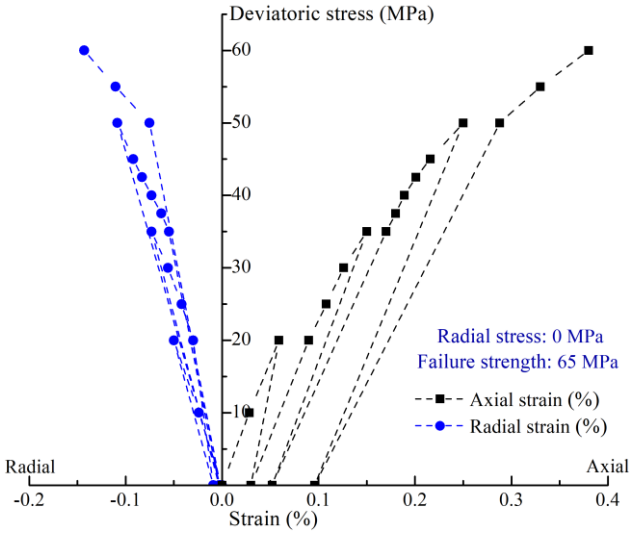

Figure 8-4: Deviatoric stress versus average radial and axial strains of the sample S1-1 on a uniaxial compression test.

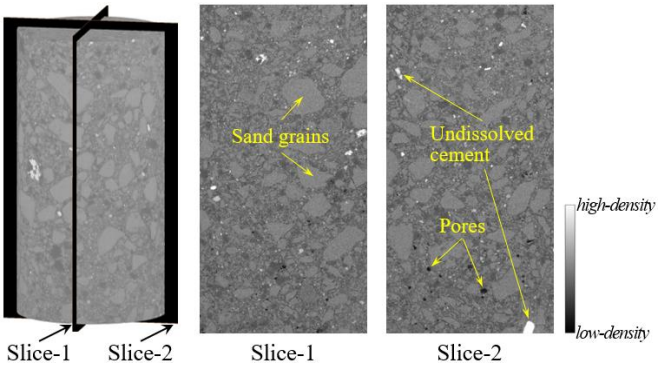

Figure 8-5: Representative grayscale images of tomographic reconstruction of two mutually perpendicular longitudinal slices.

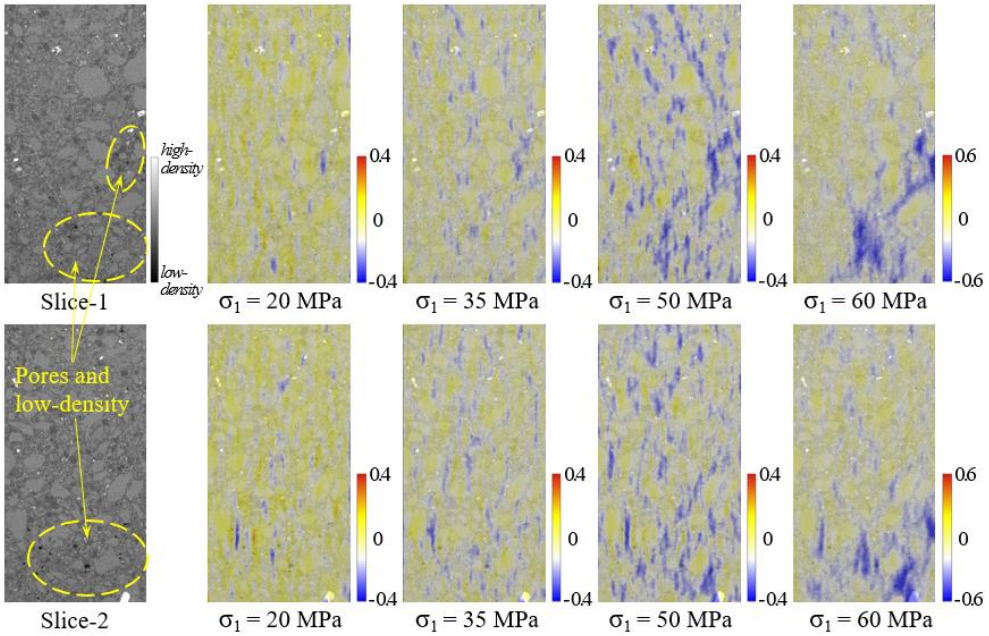

Figure 8-6: Distributions of the accumulated radial strain fields of the selected slices in sample S1-1.

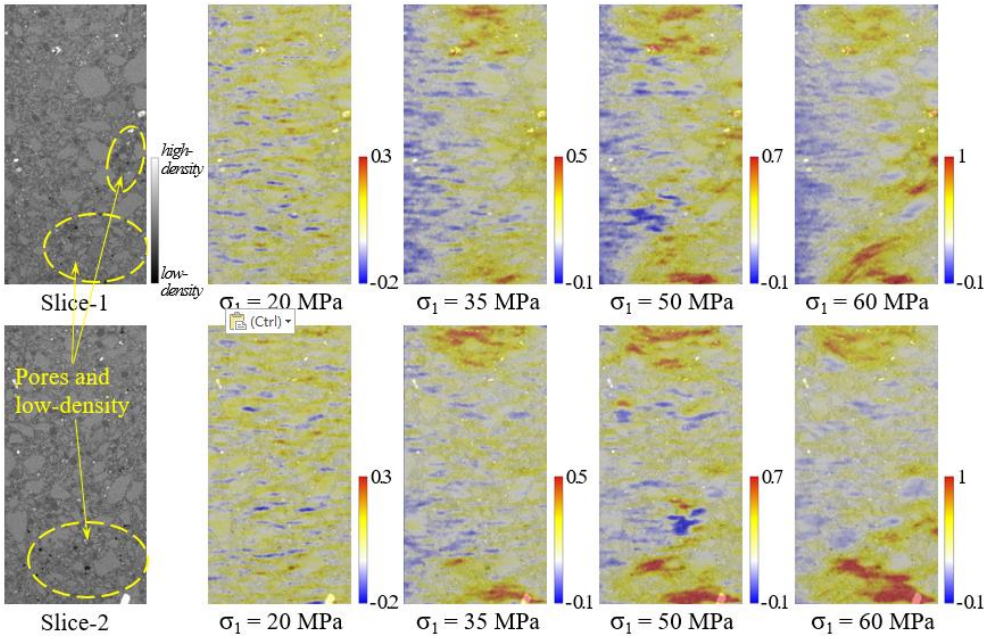

Figure 8-7: Distributions of the accumulated axial strain fields of the selected slices in sample S1-1.

As can be seen from the tomographic reconstruction of the grayscale images illustrated in Figure 8-5, the components of the mortar samples can be well differentiated at a resolution of about 7 μm. The accumulated axial and radial strain fields illustrated in Figure 8-6 and Figure 8-7 both indicate that the large deformation zones in the sample are present in the porous cement agglutinated zones. The computational element size of DVC here is 8 × 8 × 8 pixels.

To continue exploring the reasons for the abnormal radial strains, a third uniaxial compression test was performed. Figure 8-8 illustrates the stress-strain relations for the sample S1-3. The failure strengths of samples S1-2 and S1-4 are 45 MPa and 65 MPa, respectively, and their stress-strain relations as well as strain fields will be shown in the future reports. At this time, no abnormal data were found. Comparing the environments of the three uniaxial compression tests, it was preliminary determined that the primary factor for the abnormal data was the variation of temperature in the room during the experiments.

Figure 8-9 displays the global average strains of the tested sample corresponding to the temperature variations of the triaxial device (outer wall of the cell) in the X-ray micro-tomographic room on 8 March 2023. It can be seen that both the axial and radial strains in the sample present dilation, and the radial strain is stronger. Moreover, the axial and radial strains are essentially linear with respect to temperature. This explains the abnormal radial strains in the previous tests.

Subsequently, three mortar samples were conducted in triaxial compression tests. The stress-strain relations are shown in Figure 8-10 to Figure 8-12. As a reminder, the computational element size of DVC in these three tests is 4 × 4 × 4 pixels. Figure 8-11 illustrates the distributions of the accumulated radial and axial strain fields for a selected slice in sample S1-3s. Figure 8-12 and Figure 8-14 present the accumulated radial and axial strain fields of samples S1-3s and S1-5, respectively. The sample data here is not sufficient, so more repetitive tests are needed. Therefore three to five repetitions of the test will be performed for each defined conditions. With the available test data, it can be determined that confining pressure increased the failure strength of the mortar samples by approximately 25-50%.

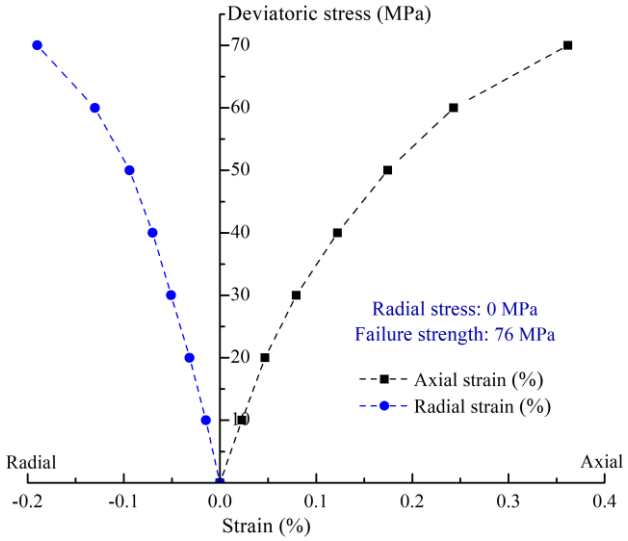

Figure 8-8: Deviatoric stress versus average radial and axial strains of the sample S1-3 on a uniaxial compression test.

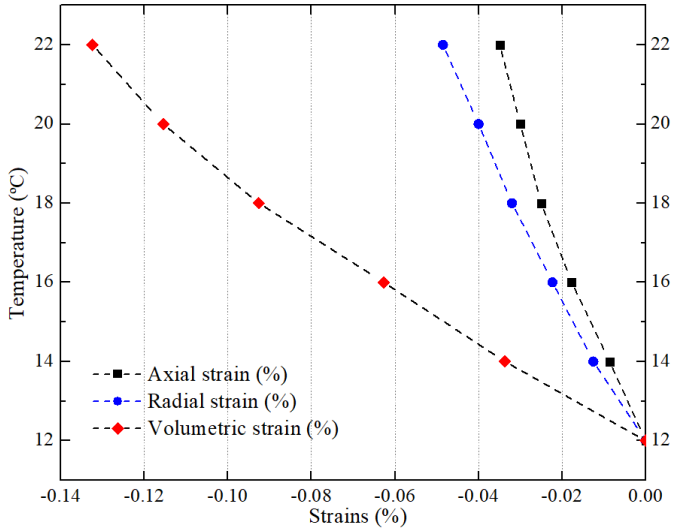

Figure 8-9: Variations of axial and radial strains in the sample S1-4 in response to temperature.

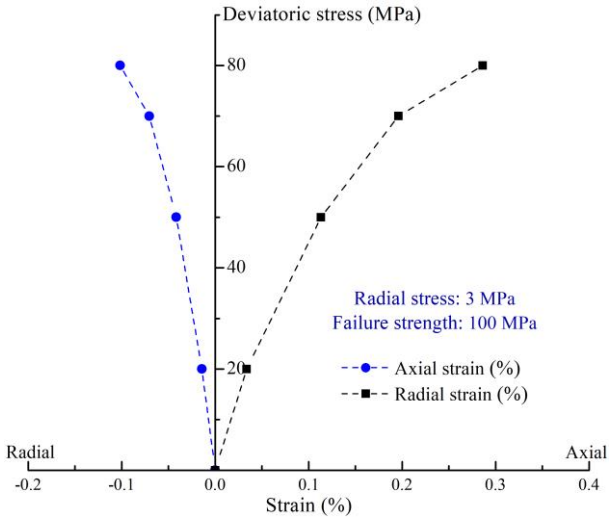

Figure 8-10: Deviatoric stress versus average radial and axial strains of the sample S1-3s on a triaxial compression test.

As can be seen in Figure 8-11, the initial cracks (marked by the yellow dashed line) are present in the middle and bottom left corner of the selected slice. During the entire loading process, the initial crack in the middle of the sample was continuously compressed in the axial direction and generated a large axial compressive strain. Meanwhile, in the area of the bottom left corner, a large compressive strain is generated in the axial direction, but also a large dilation strain in the radial direction. For the strain fields of the sample (in Figure 8-12), significant compression bands formed in the initial crack zones can be seen. The localised zone of large deformation that occurred at the top part of the sample is probably due to the defects that were produced in the sample during the machining procedure.

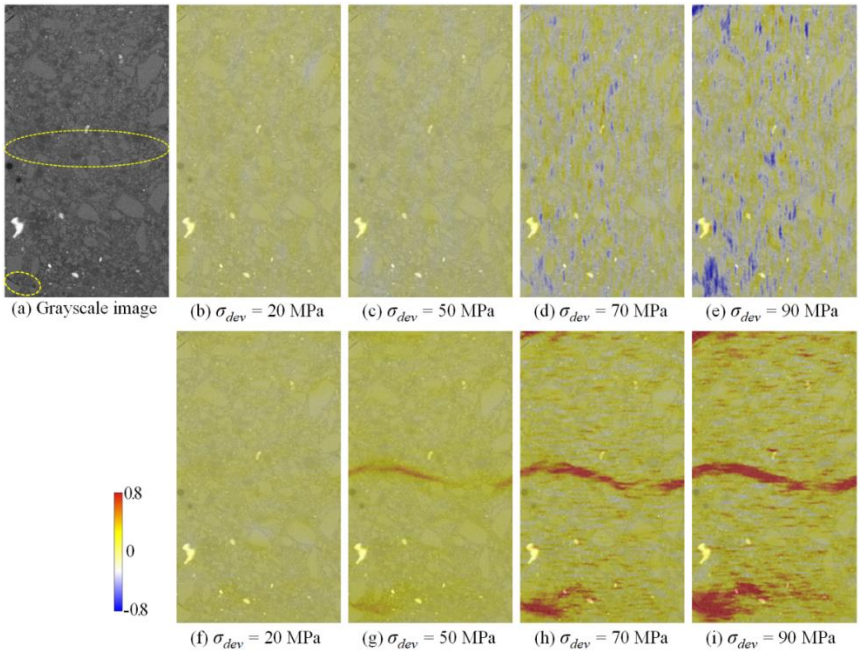

Figure 8-11: Distributions of the accumulated radial (b~e) and axial (f~i) strain fields of the selected slice in sample S1-3s.

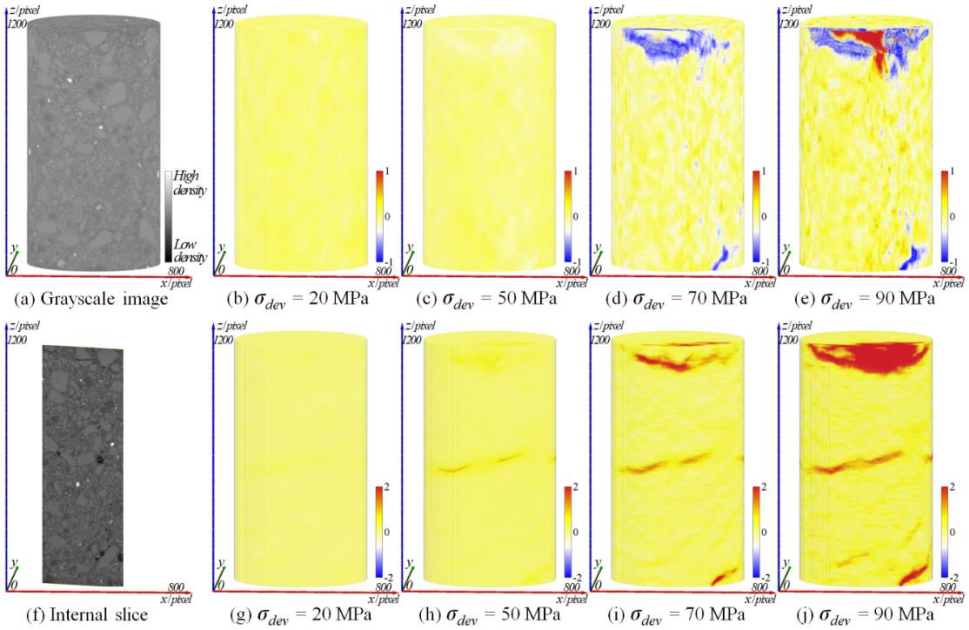

Figure 8-12: Distributions of accumulated radial (b~e) and axial (g~j) strain fields (%) in sample S1-3s.

Samples S1-5 and S1-6 were tested under the same conditions and fortunately the same failure strength was acquired for both triaxial tests. The stress-strain relations are shown in Figure 8-13 and Figure 8-15, respectively. Figure 8-14 shows the accumulated radial and axial strain fields for samples S1-5. Layered compression bands can be viewed in the axial strain fields. A remarkably large dilation zone in the radial

strain field at the bottom part of the sample is observed at a loading level close to the peak strength. The axial strain field at this point exhibits significant cross-compression bands. An internal slice of the sample (see Figure 8-14e) shows the presence of very large initial holes (up to 1 mm in diameter) at the bottom of the sample. This should be the immediate factor contributing to the extraordinarily large deformation in the sample.

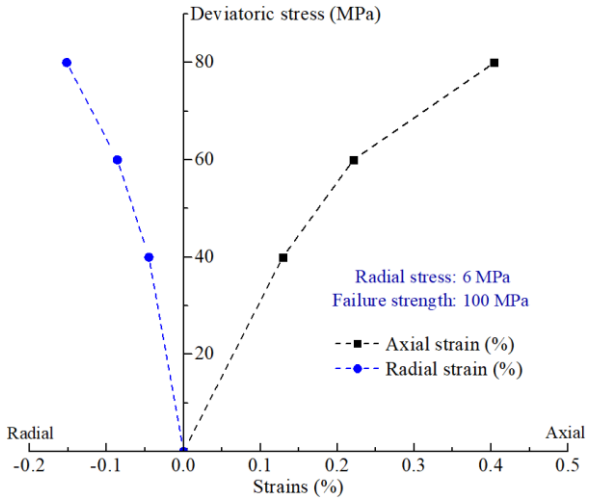

Figure 8-13: Deviatoric stress versus average radial and axial strains of the sample S1-5 on a triaxial compression test.

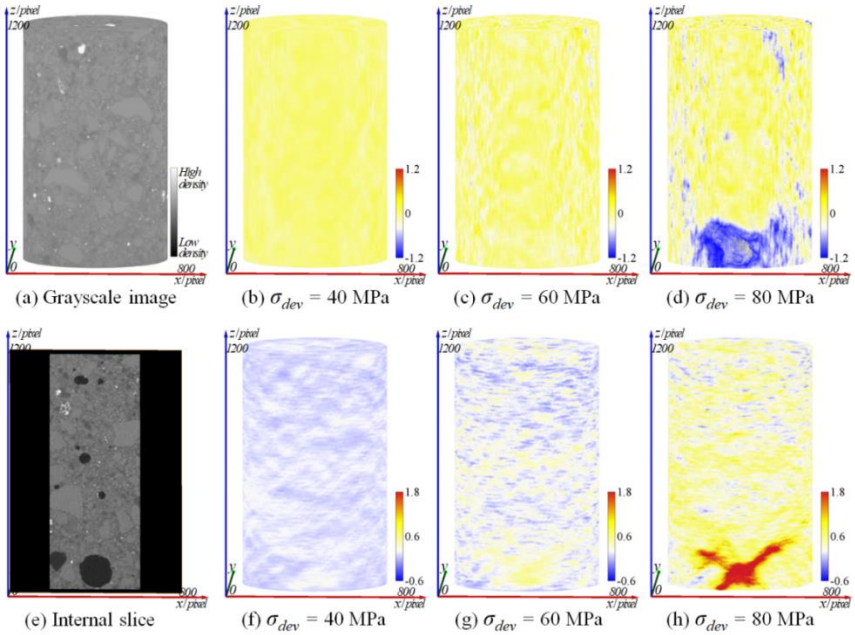

Figure 8-14: Distributions of accumulated radial (b~d) and axial (f~h) strain fields (%) in sample S1-5.

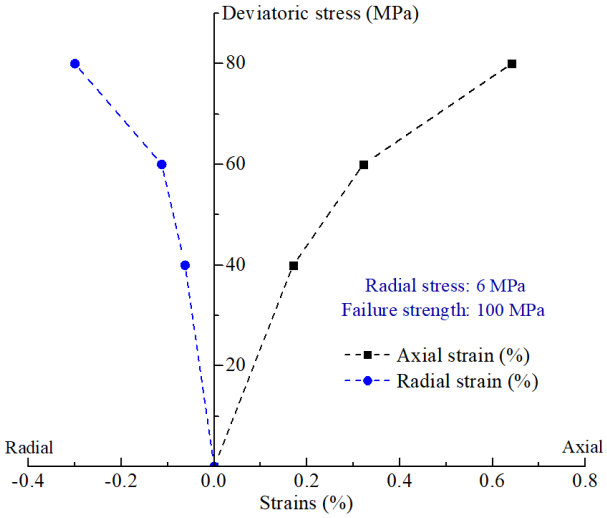

Figure 8-15: Deviatoric stress versus average radial and axial strains of the sample S1-6 on a triaxial compression test.

Two uniaxial tests and one triaxial test were performed on the medium carbonated samples. The stress-strain relations for the two uniaxial tests are shown here in Figure 8-16 and Figure 8-18, and the accumulated radial and axial strain fields for Sample S2-4 are displayed in Figure 8-17. For Sample S2-4s it was not possible to obtain the scanned images under high stress due to a technical issue, therefore DVC calculations could not be performed. The uniaxial failure strengths of samples S2-4 and S2-4s were 60 MPa and 70 MPa, respectively, which were slightly higher than the uncarbonated samples in general. More repeated tests are necessary for comparison. More mechanisms and more in-depth analyses require time. The results of the triaxial test on sample S1-1s will be shown in the future reports.

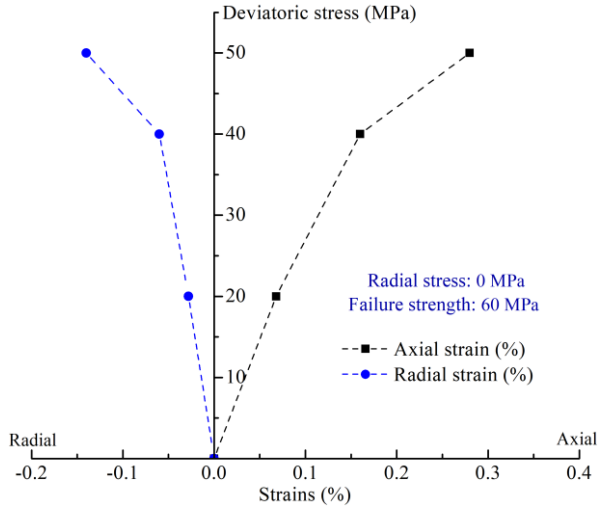

Figure 8-16: Deviatoric stress versus average radial and axial strains of the sample S2-4 on a triaxial compression test.

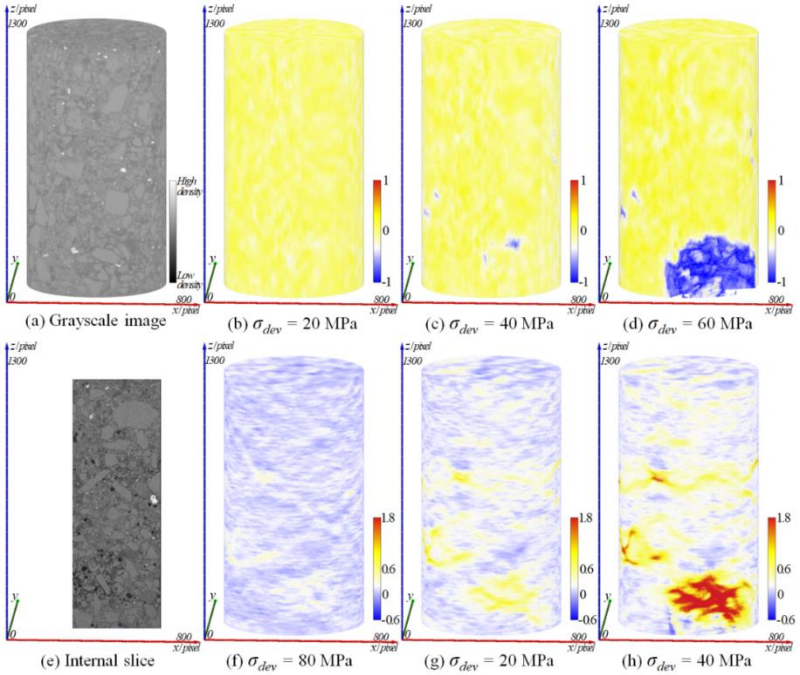

Figure 8-17: Distributions of accumulated radial (b~d) and axial (f~h) strain fields (%) in sample S2-4.

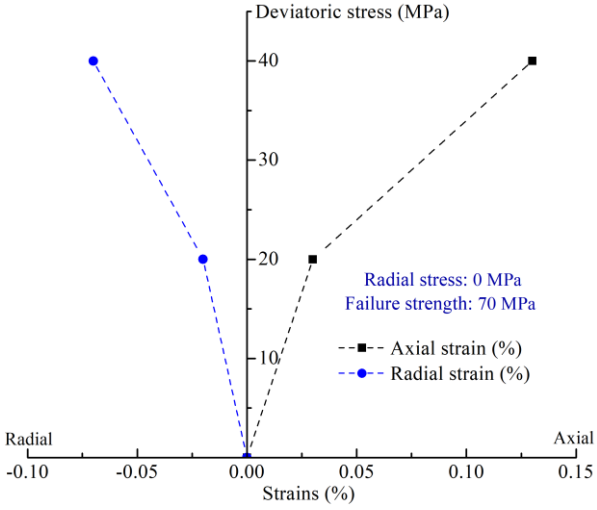

Figure 8-18: Deviatoric stress versus average radial and axial strains of the sample S2-4s on a triaxial compression test.

A total of one uniaxial and three triaxial tests were carried out on the full carbonated mortar samples. One of the triaxial tests with a confining pressure of 6 MPa failed to acquire images at high deviatoric stress due to a technical issue.

Figure 8-19 illustrates the results of the uniaxial test. The sample was maintained at a deviatoric stress of 100 MPa for approximately 3 minutes before failure. The full carbonated mortar sample showed an average increase in uniaxial peak strength of about 40% with respect to the uncarbonated samples.

The results of two triaxial tests with a radial stress of 3 MPa are presented in Figure 8-20 and Figure 8-21. The failure strengths of the two samples are almost the same, 99 MPa and 100 MPa, however they are a little lower than we expected. It could be that there are some defects in the samples contributing to the low failure strength. Figure 8-22 presents the accumulated radial and axial strain fields of sample S1-5c. The initial crack located at the middle of the sample resulted in a horizontal compressive band in the axial strain. The large strains at the bottom part of the sample should be a result of a combination of processing defects and weak zones in the sample. The strain fields of a vertical

longitudinal slice in sample S1-5c are displayed in Figure 8-23. A horizontal initial crack (marked by yellow line) and a huge hole (marked by black line) can be observed in the greyscale image of the selected slice. A large strain compression band was generated around the initial crack. The presence of the huge hole caused some dilatation bands to appear in the surrounding zone.

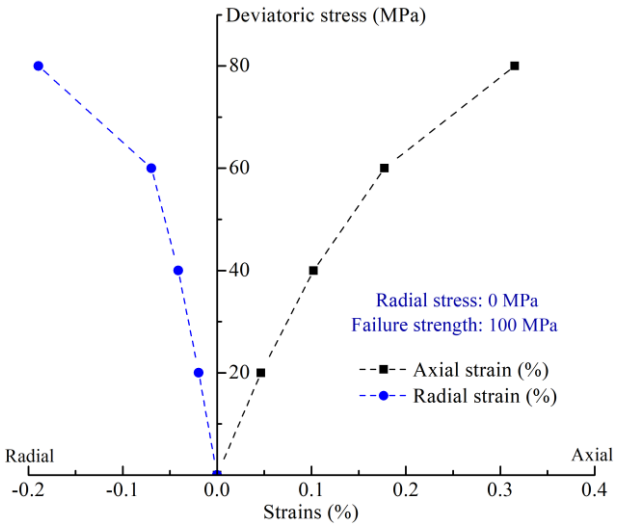

Figure 8-19: Deviatoric stress versus average radial and axial strains of the sample 1-2t on a triaxial compression test.

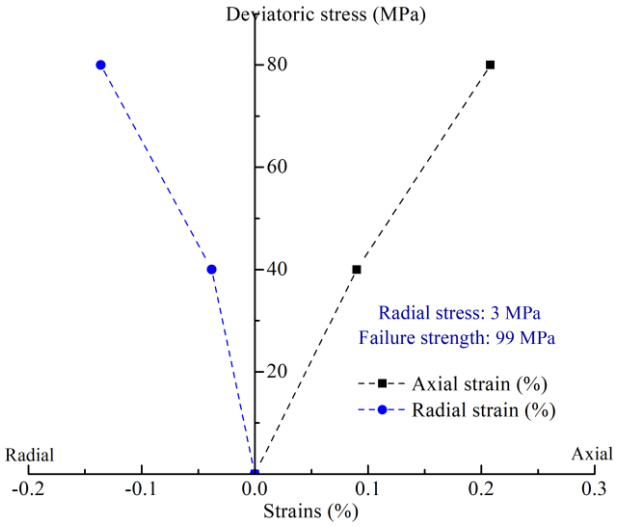

Figure 8-20: Deviatoric stress versus average radial and axial strains of the sample S1-7c on a triaxial compression test.

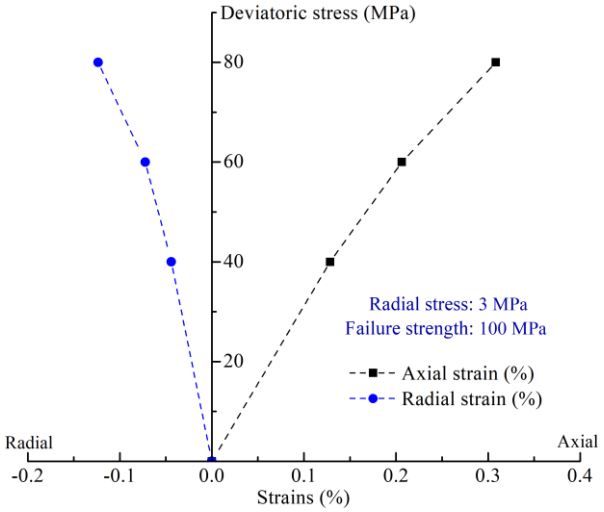

Figure 8-21: Deviatoric stress versus average radial and axial strains of the sample S1-5c on a triaxial compression test.

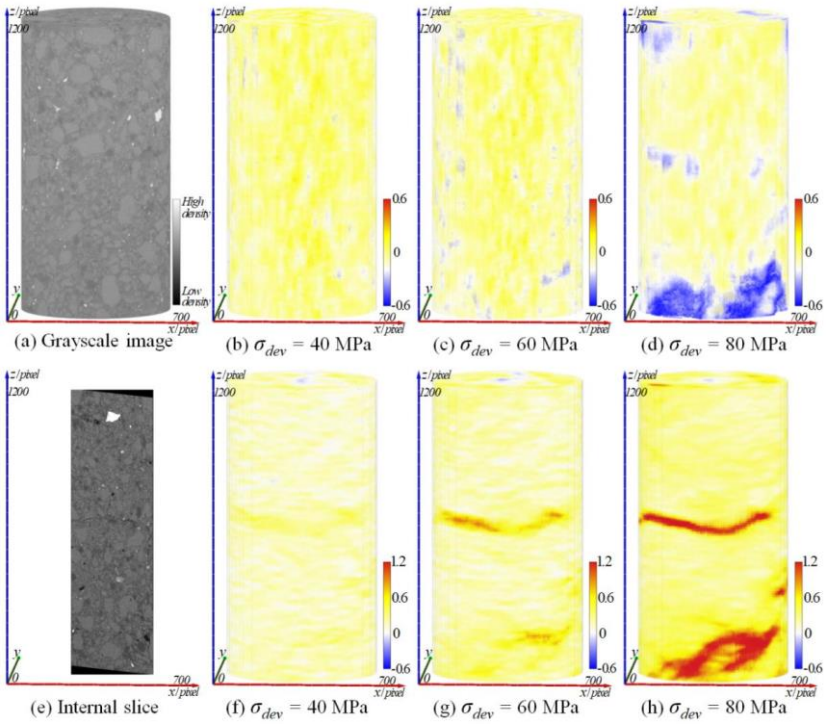

Figure 8-22: Distributions of accumulated radial (b~d) and axial (f~h) strain fields (%) in sample S1-5c.

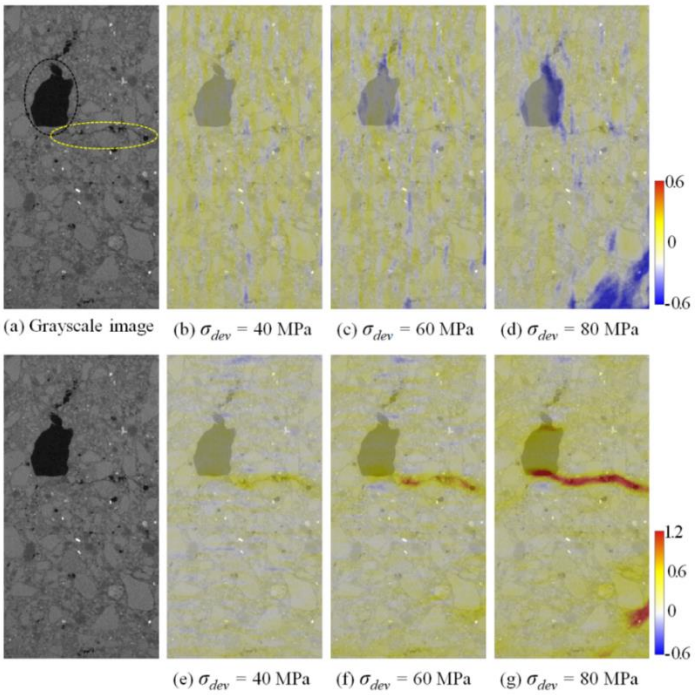

Figure 8-23: Distributions of the accumulated radial (b~d) and axial (e~g) strain fields of the selected slice in sample S1-5c.

9. Summary of meso-mechanical tests

9.1 Further experimental arrangements

Some difficulties have been encountered in the production and carbonation of small sized mortar samples, as well as in X-ray micro-tomographic scans. Fortunately, the difficulties have now been overcome. In the upcoming time, we will continue to conduct uniaxial, triaxial and creep compression tests on mortar samples with different carbonation levels.

9.2 Conclusions

Although not all the tests have been completed, there are some simple conclusions that we can make.

(1) In general, small sized mortar samples are affected by temperature variations in a non-negligible way. Therefore, temperature stability needs to be controlled as well as possible during all tests. Depending on the conditions in the laboratory, we keep the temperature for all tests at 23±1 °C.

(2) Carbonation of small sized mortar samples takes more time and is more complex than anticipated. Complete carbonation of small mortar samples takes more than four weeks.

(3) Since the processes of small sized samples are more complex compared to large samples, unavoidable defects often develop. These defects generally decrease the failure strength of the tested sample. Many repetitive tests under the same conditions are necessary.

(4) The influence of carbonation in samples on mechanical properties is objective. The impact on the strength of the sample in instantaneous mechanical tests is positive. To quantify these values more experimental data are required.

(5) The failure pattern of the samples is important. This will be presented in future reports.

Part Ⅲ Chemo-mechanical experiment

10. Subtask, aim and the focus of the experimental activities

In the framework of the IMCB project (Impact of calcareous water on chemo-MeChanical Behaviour of concrete), which aims to understand the chemo-mechanical impact of calcareous water on the low-pH cementitious matrix, IRSN started a study to estimate the potential difference in results obtained under controlled conditions and ones made with the industrial scale equipment. On one hand, HCP was cast in the laboratory, and on the other hand, concrete samples and massive concrete structures were cast outside experimental platforms. After the hydration period, samples were immersed in a high volume of natural calcareous ground water. Periodic characterization was performed by SEM-EDS, µ-CT, XRD and micro/nano-indentation.

11. Size of samples/system setup, cement paste recipe/pore water; perturbations

Two experimental devices were used. The first system set up in December 2018 in the IRSN underground research laboratory (URL) in Tournemire (IMCB-TR) was only composed of centimetric samples. The second one (IMCB-ODE), started in October 2019 and located in the ODE platform of Cadarache (South of France), was focused on macroscopic scale. In both cases, the composition of the attack solution was equivalent to natural calcareous ground water from the Cernon fault in the URL of Tournemire. Table 11-1 details the concentration of the main chemical elements present in this water.

Table 11-1: Chemical composition of water from the Cernon fault.

Chemical element	Concentration mmol/L / pH
Ca^{2+}	1.91
HCO_3^-	5.9
Mg^{2+}	0.82
SO_4^{2-}	0.06
pH	8.2

The Low-pH formulation employed is called T3 and contain 67.5% of CEM IIIA Rombas 52.5L and 32.5% of silica fume CONDENSIL S95 DM. Sand and aggregates were calcareous from the stone quarry of Boulonnais. The aggregate on binder ratio and the sand on binder ratio were respectively equal to 2.56 and 2.27. The composition of low-pH HCP (hardened cement paste) and concrete is inspired by the work of (Codina et al., 2007) and (Bach et al., 2007). The proportion of each constituent is detailed in Table 11-2.

HCP samples of IMCB-TR were cast with deionized water in controlled laboratory conditions and kept for 2 years in a sealed bag at 20°C. The concrete samples were mixed with tap water in a concrete plant, then cast in the outside ODE platforms. A deflocculated process of silica fume was carried out before the mixing part. To replicate the sealed bag condition, concrete blocks of IMCB-ODE were wrapped with stretch film for a year. Concrete samples of IMCB-TR were kept in a sealed bag for a year in controlled laboratory conditions.

In both experiments, XRD and ATG analysis confirmed that the hydration period was long enough to remove any trace of portlandite from the cement matrix.

Table 11-2: Composition of compounds of hardened cement paste and concrete.				
Compounds			HCP (kg/m3)	Concrete (kg/m3)
Cement: CEM III/A 52.5L Rombas	Mineral composition (g/100g of anhydrous cement)		826	256.7
	C3S	15.9		
	C2S	2.6		
	C3A	2.4		
	C4AF	1.9		
	Slag	42.1		
	Anhydrite	4.1		
Silica Fume: CONDENSIL S95 DM			398	125
Superplasticizer			16	6.02
Water on cement ratio (%)			0.43	0.403
Sand: 0/4 Boulonnais (HR: 8.3%)			0	943.3
Aggregates 4/12 Boulonnais (HR: 1.5%)			0	980

12. Description of the experimental methods

In IMCB-TR, the naturally calcareous water was diverted into degradation tanks containing HCP and concrete. The samples are cylinders of three centimetres in diameter and one centimetre high. A waterproof resin (Resoltech 3030) was applied to each slice to force unidirectional diffusion. Low flow is applied in the degradation tanks to maintain continuous renewal of the solution.

In IMCB-ODE, three low-pH concrete blocks 1×1×1.7m were built from a mix coming from a concrete plant. A year later, a degradation tank was mounted around these blocks. 4300 litres of a synthetic solution equivalent to that from the Cernon fault was introduced into the tank. Acid pH regulation and salt additions were carried out weekly to ensure the stability of the solution. Sampling was carried out by coring the block and the residual hole was plugged with resin. Coring was carried out in an area far enough away from the corners of the block to assume a unidirectional attack. As the low-pH formulation changes according to the block, we assumed that, due to pH regulation and salt addition, no interaction occurred between the blocks. This study focuses on the block cast with the low-pH formulation called T3.

Every two months, a sample is extracted from IMCB-TR or IMCB-ODE. It is divided into several subsamples which are prepared differently according to the analysis for which they are intended.

The XRD analyses presented in this study were carried out with an Aeris Research Edition diffractometer from Malvern-Panalytical in θ−2θ configuration, under CuKα radiation (λ = 1.54 Å) with a divergence slot of 0.5° and a rotation platform. The diffractogram profiles were performed on "solid sample" (Planel et al., 2006). This technique aims to acquire all the crystallographic data from the degraded surface to the sound part of the cementitious material. The contact surface is first analysed with XRD. Once the

diffractogram is obtained, the sample is polished a little, then reanalysed. This operation is repeated sufficient number of times to reach the sound part of the sample.

The µ-CT analyses were carried out on a Brüker SkyScan 1173 equipped with a 2k pixel detector operating at 130kV and 61 µA. The acquisition parameters are a 0.1° rotation pitch, a 10-averaging frame, a 360° rotation and a 20 µm pixel size. Following the reconstruction, a median filter of radius 2 was applied. A K-means deconvolution (Hartigan et al., 1979) was then carried out on sound concrete samples to highlight a threshold in 4 parts: aggregates, healthy matrix, a macroporous zone and pores greater than 20 µm.

SEM-EDS analyses were carried out on carbon metallized polished sections. The acquisition was performed on SEM Hitachi S3500N with two EDS Brüker 5030 XFlash at 15 keV with x80 magnification. The pixel size is 3 µm, at the limit of the interaction pair for this type of material (Bentz et al., 1999). The average number of photons per pixel is greater than 4000, allowing rework of signals from hyperspectral images. Post-processing was applied to concrete EDS analysis to exclude aggregates from the hyperspectral image, thus focusing only on the cementitious matrix. The intensities presented in this paper are always expressed in the intensity ratio per pixel. This implies that a pixel displaying for an element an intensity ratio of 0.2 contains 20% of this element in terms of intensity. The intensity profiles were calculated by averaging the intensity ratios in the direction parallel to the degradation front. Each point of these profiles results from the average of about 500 pixels.

The evolution of mechanical properties was estimated for HCP and concrete by micro-indentation measurements with an Anton & Paar NHT3 nano-indentor equipped with a Berkovitch tip. The tests were carried out on the same polished section as that used for the SEM-EDS analysis. Experiments were force-controlled in quasi-static mode according to the method developed by Oliver & Pharr (Pharr et al., 1992). The maximum force was set at 200mN with a loading and unloading speed of 100 mN/s.

8 grids of 3×5 indents with grid spacing of 100µm apart were realized in the degraded zone of a concrete that had been immersed for 8 months in the IMCB-ODE. The 8 grids were then grouped together to be analysed according to the distance from the interface.

Nano-indentation maps were plotted for HCP with the same device. The grid nano-indentation technique was used to map the mechanical property distribution of the sound low-pH HCP. Tests were displacement-controlled with nanoindentation depth equal to 0.30 µm to focus on the mechanical properties of the HCP constituents without macroscale effect (Hu et al., 2015). Poisson's ratio was assumed to be constant and equal to 0.24. A loading and unloading speed of 12mN/s was applied for each indent. Quasi-static measurement with Olivier & Phar technique (Pharr et al., 1992 and Oliver et al., 2004) was performed four times on a 35 x 35 grid with grid spacing of 10 µm.

Compressive tests were performed on concrete samples according to the NF EN 12390-13 standard, with 3 LVDT sensor strain measurements arranged at 120° on the lateral surface.

Porosity accessible to water was carried out by weighing the sample from saturation to dry state according to the protocol NF P 18-459 (AFNOR NF, 2010). A cylindrical specimen with a diameter of 7 cm and a height of 1 cm was subjected to two consecutive steps. First, the sample is saturated with MilliQ water for 48 hours then heated at 105°C until constant weight is reached. The dry state of the samples is achieved when the relative mass loss between two weighs of the sample spaced 24 hours apart at 105°C is less than 0.05%.

13. Experimental results

The first aim of this study was to provide insights for understanding the chemo-mechanical behaviour of a low-pH cementitious matrix in contact with calcareous ground water.

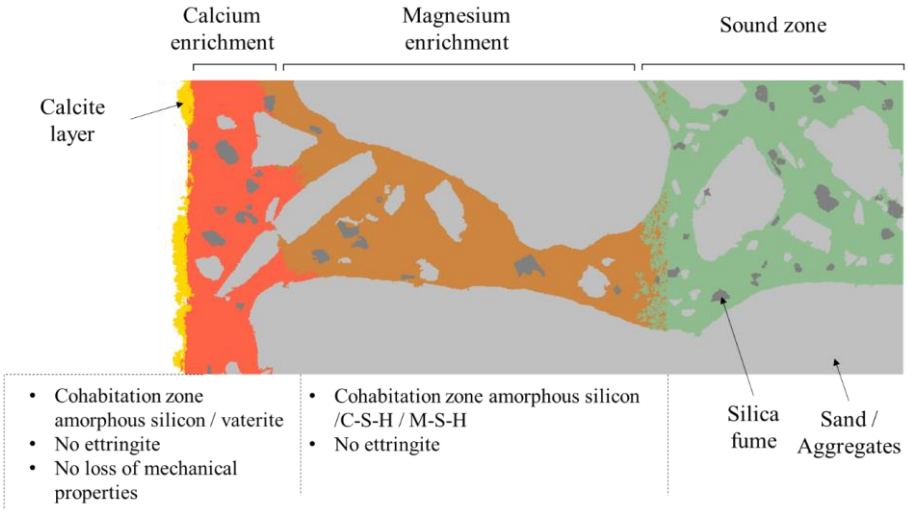

Figure 13-1: Illustrative diagram of the degradation scenario proposed to explain the alteration of low-pH cementitious matrix in contact with calcareous water.

The experimental campaign, coupled with numerical simulation, highlights, as illustrated by the Figure 13-1, the following mineralogical changes:

- At the interface, a crust of calcium carbonate is visible.
- The first hundred microns are marked by the presence of calcium enrichment and the presence of amorphous silica. Vaterite has been identified in this area. The presence of vaterite counterbalances the amorphous silica offering a high Young's modulus (Figure 13-2). A flaking phenomenon in this zone is suspected, likely due to the low Young's modulus of amorphous silicon.
- Magnesium enrichment is observed upstream of the previous zone. Despite the low concentration of the attack solution, the model and SEM-EDS measurements show that the magnesium enrichment can, in some cases, reach 20% of the volume ratio of the material. The low mechanical properties of the magnesian phases usually observed in low-pH matrices raise the question of the durability of this zone.

The second objective of this study is to estimate the potential deviation of results between a study made in controlled conditions and another in uncontrolled industrial conditions. The conservation protocol seems to have a significant impact on the chemical response of the cementitious materials. A high porous zone appears at the interface in large concrete blocks cured outside and wrapped with stretch film. The modification of transport properties in this zone changes the degradation scenario. In the case of cementitious materials cured in controlled conditions, the attack solution induces a layer of calcium carbonates, which tends to close the porosity. No degradation is noticed in the cement matrix. In the high porous zone, the formation of two large enrichment zones is observed, one in calcium at the interface and another further upstream in magnesium. The evolution of these zones raises some concerns regarding the potential flaking in the calcium carbonates zone and the low Young's modulus of the magnesium phases suspected to precipitate in the magnesium enrichment zone. However, the change observed in the degradation scenario should be limited to the high porous zone, without impacting the integrity of the concrete structure.

More details about this study can be found in the paper of (Neji et al., 2023).

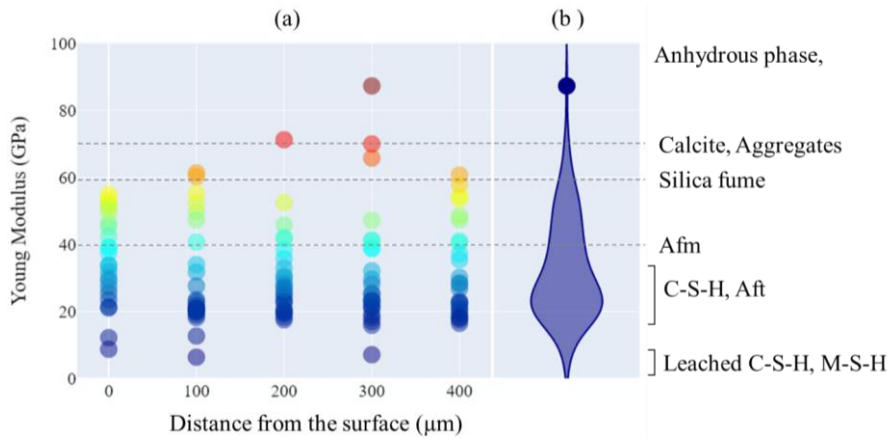

Figure 13-2: (a) Distribution of Young's moduli measured by micro-indentation as a function of depth and (b) global violin diagram for a low-pH T3 concrete immersed for 8 months in IMCB-ODE. The colormap is proportional to the Young's moduli.

14. Links with multiscale models

A Numerical work was performed in this study to compared behaviour of HCP and concrete at micro-scale, specially in term of hydration calculation and reactive transport (Neji et al., 2023).

15. General Conclusions

In this deliverable, comprises description of experimental approaches and an initial synthesis of experimental data which can be used for the testing the multiscale models developed in Task 4. Three aspects are addressed in detail: the microstructural evolution of cement-cement paste due to chemical degradation, mechanical responses of mortar at microscopic scale and chemo-mechanical coupling effects.

The collaborative work by Empa and PSI has focused on chemo-mechanical characterization of cement pastes microstructure. Within the project, a new reaction cell for diffusion and accelerated degradation experiments. Mortar specimens were exposed to Opalinus Clay pore solution, undergo diffusion and degradation experiments at 40°C. The Initial HTO diffusion results revealed potential effects of carbonation on mortar pore structure. This development lays the groundwork for in-depth investigations of cement paste microstructure. The available HTO breakthrough curves can be used for the validation of transport models. The diffusion and degradation experiments are underway, revealing early insights into potential carbonation effects. As the experiments progress, further analyses will refine models and contribute valuable data to the broader context of cement degradation. Moreover, RUS measurements, X-ray tomography, and SEM-EDX mapping at the starting time point of the degradation experiments have also been performed. The data processing and result analyses will be done after the final report. Sampling and comprehensive characterizations for the following 4-5 time points will be continued.

The LaMcube-CNRS has successfully performed a series of uniaxial and triaxial compression tests with microtomography monitoring. Three-dimensional distribution of axial and radial strains as well as sample failure pattern are determined. According to the results obtained so far, some preliminary concluding remarks can be formulated. The complete carbonation of mortar samples is longer than expected and takes more than four weeks. The fabrication of small sized samples is a complex process and it is susceptible to introduce unavoidable micro-cracks in samples. These initial defeats can affect the subsequent mechanical responses of the tested sample. The effects of carbonation on mechanical properties are clearly confirmed. In general, the carbonation enhances the failure strength of the samples. Additional tests are undergoing and will confirm the preliminary results. In particular, the influence of carbonation of the failure pattern of the samples will be investigated. The experimental results obtained in this part, precisely stress-strain curves and 3D distribution of local strain fields, provide a very interesting dataset for multiscale modelling.

The work done by the IRSN aims to understand the chemo-mechanical impact of calcareous water on the low-pH cementitious matrix. They have studies both HCP samples cast in the laboratory and concrete samples and massive concrete structures cast in field scale experimental platforms. The hydrated samples were immersed in a high volume of natural calcareous ground water, and then periodically analysed by using SEM-EDS, µ-CT, XRD and micro/nano-indentation. The preliminary mains results are as follows. There is a formation of a crust of calcium carbonate, providing a high Young's modulus. But a flaking phenomenon in this zone is suspected, likely in relation of the low Young's modulus of amorphous silicon. The Magnesium enrichment is observed and can reach 20% of the volume ratio of the material. However, the conservation protocol seems to have a significant impact on the chemical response of the cementitious materials, and then affects the mechanical properties.

References

AFNOR. Essai Pour Béton Durci—Essai de Porosité et de Masse Volumique—NF P18-459[J]. 2010.

Attix F H. Introduction to radiological physics and radiation dosimetry[M]. John Wiley & Sons, 2008.

Avril S, Bonnet M, Bretelle A S, et al. Overview of identification methods of mechanical parameters based on full-field measurements[J]. Experimental Mechanics, 2008, 48: 381-402.

Bach T, Pochard I, Cau-Dit-Coumes C, et al. Prediction of long-term chemical evolution of a low-pH cement designed for underground radioactive waste repositories[J]. Cement-Based Materials for Nuclear Waste Storage, 2013: 239-249.

Bentz D P, Stutzman P E, Haecker C J, et al. SEM/X-ray imaging of cement-based materials[J]. Proceedings of the 7th Euroseminar on Microscopy Applied to building Materials, 1999: 457-466.

Besnard G, Hild F, Roux S. “Finite-element” displacement fields analysis from digital images: application to Portevin–Le Châtelier bands[J]. Experimental mechanics, 2006, 46: 789-803.

Buljac A, Jailin C, Mendoza A, et al. Digital volume correlation: review of progress and challenges[J]. Experimental Mechanics, 2018, 58: 661-708.

Codina M, Cau-dit-Coumes C, Le Bescop P, et al. Design and characterization of low-heat and low-alkalinity cements[J]. Cement and Concrete Research, 2008, 38(4): 437-448.

Hu C, Li Z. A review on the mechanical properties of cement-based materials measured by nanoindentation[J]. Construction and Building Materials, 2015, 90: 80-90.

Kak A C, Slaney M. Principles of computerized tomographic imaging[M]. Society for Industrial and Applied Mathematics, 2001.

Latiere H J, Mazerolle F. The X-ray scanner. A tool for the examination of the intravoluminal crystalline state of aluminum[J]. Engineering Fracture Mechanics, 1987, 27(4): 413-463.

Limodin N, Rougelot T, Hosdez J. Isis4d—in situ innovative set-ups under x-ray microtomography[J]. 2013.

Luraschi P, Gimmi T, Van Loon L R, et al. Evolution of HTO and 36Cl− diffusion through a reacting cement-clay interface (OPC Paste-Na montmorillonite) over a time of six years[J]. Applied geochemistry, 2020, 119: 104581.

Neji M, Dewitte C, Durville B. Influence of porosity network on the chemo-mechanical evolution of low-pH cementitious materials subjected to calcareous attack[J]. Construction and Building Materials, 2023, 405: 133313.

Oliver W C, Pharr G M. Measurement of hardness and elastic modulus by instrumented indentation: Advances in understanding and refinements to methodology[J]. Journal of materials research, 2004, 19(1): 3-20.

Pharr G M, Oliver W C. Measurement of thin film mechanical properties using nanoindentation[J]. Mrs Bulletin, 1992, 17(7): 28-33.

Planel D, Sercombe J, Le Bescop P, et al. Long-term performance of cement paste during combined calcium leaching–sulfate attack: kinetics and size effect[J]. Cement and Concrete Research, 2006, 36(1): 137-143.

Seghir R, Witz J F, Coudert S. YaDICs-Digital Image Correlation 2/3D software, 2014[J]. URL http://yadics.univ-lille1.fr.

Shi H L, Hosdez J, Rougelot T, et al. Analysis of local creep strain field and cracking process in claystone by x-ray micro-tomography and digital volume correlation[J]. Rock Mechanics and Rock Engineering, 2021, 54: 1937-1952.

Shi H L, Rougelot T, Xie S Y, et al. Investigation of strain fields and anisotropy in triaxial tests on Callovo-Oxfordian claystone by X-ray micro-tomography and digital volume correlation[J]. International Journal of Rock Mechanics and Mining Sciences, 2023, 163: 105330.

Shi H, Hosdez J, Rougelot T, et al. Digital volume correlation applied to X-ray micro-tomography images in uniaxial creep tests on anisotropic clayey rock[J]. Applied Sciences, 2020, 10(14): 4898.

Sutton M A, Wolters W J, Peters W H, et al. Determination of displacements using an improved digital correlation method[J]. Image and vision computing, 1983, 1(3): 133-139.

U. Mäder, E. Bernard, CI-D Experiment: Synthetic high-pH pore water and start of fluid circulation. Mt. Terri URL Technical Note TN-2020-51, 2018.

Zadler B J, Le Rousseau J H L, Scales J A, et al. Resonant ultrasound spectroscopy: theory and application[J]. Geophysical Journal International, 2004, 156(1): 154-169.